Wetting and evaporation of multicomponent droplets

Wetting and evaporation of multicomponent droplets

Zhenying Wang [a,b,*], Daniel Orejon [b,c], Yasuyuki Takata [b,c,d], Khellil Sefiane [c]

[a] *Department of Aeronautics and Astronautics, Kyushu University, Nishi-Ku, Motooka 744, Fukuoka 819-0395, Japan*
[b] *International Institute for Carbon-Neutral Energy Research (WPI-I2CNER), Kyushu University, Fukuoka 819-0395, Japan*
[c] *Institute for Multiscale Thermofluids, School of Engineering, University of Edinburgh, Edinburgh EH9 3JL, UK*
[d] *Department of Mechanical Engineering, Kyushu University, Nishi-Ku, Motooka 744, Fukuoka 819-0395, Japan*

ARTICLE INFO

ABSTRACT

Wetting and evaporation of sessile droplets are ubiquitous in nature and of importance to many industrial and everyday processes. While most of the research on sessile droplets has been constraint to single component droplets, complex multicomponent droplets are in fact the most common systems in natural and industrial fields. Multicomponent droplets show diverse behaviors as the concentration of the different components varies in both the liquid and the gas phases. The nonuniform distribution of different components leads to surface tension gradient and affects the wetting dynamics. Additionally, some ubiquitous behaviors can be induced by the preferential evaporation of more volatile components, and by actively tuning the vapor field by adjacent droplets or via external vapor sources. In this paper, we review the underlying physical and physicochemical mechanisms of multicomponent droplets during wetting and spreading, induced by evaporation and/or mediated by the vapor field. Especially we focus on volatile multicomponent droplets and exclude the colloidal or nanofluids droplets which have been reviewed in existing papers. We overview the droplet wetting dynamics, the interfacial mass flux, the droplet lifetime and the flow patterns of these complex droplets. The available experimental and numerical methodologies to date are also summarized, including the application conditions, accuracy, resolution and limitations from the experimental aspect; as well as the main assumptions, mathematical methods and corresponding reliability from the numerical aspect. Last we discuss the significance of exploiting the interacting mechanisms with complex droplets, and point out the innovation potentials in cutting-edge applications including 3D printing, self-cleaning, digital microfluidics, cellular sorting and biomedical diagnosis, amongst others.

Contents

* Corresponding author at: Department of Aeronautics and Astronautics, Kyushu University, Fukuoka 819-0395, Japan.
   E-mail address: zhenying.wang@aero.kyushu-u.ac.jp (Z. Wang).

1. Introduction

When a finite volume of liquid gets in contact with a solid surface, it typically adopts a predetermined shape depending on the physical and chemical properties of the solid, the liquid and the surrounding gas. Liquid droplets, which can be identified as one of the most common morphologies adopted by a fluid on a solid surface in nature (opposed to liquid films), do also play a paramount role in many industrial processes, ranging from inkjet printing [1], spray cooling [2], thin film coating [3], to DNA stretching [4] and disease diagnosis [5]. In the late nineteenth century, Scottish scientist James Clerk Maxwell derived the first droplet evaporation model based on the diffusion of the vapor [6]. In this model, Maxwell considered the simplest case where a motionless spherical bulb of pure water contacts with infinite uniform bulk air. In 1915, Langmuir proposed the presence of a rapid concentration jump of water vapor near the liquid–gas interface of an evaporating droplet [7]. Thereafter, by accounting for the effect of concentration change in the gas phase, the evaporation rate was approximated by the interchange of molecules within a thin layer adjacent to the droplet interface, and then by the diffusion of the vapor described by Fick's equation [8]. The above earlier investigations considered a sessile droplet suspended in air. In 1977 though, Picknett and Bexon [9] observed and introduced the process of droplet evaporation on a solid surface. They identified two extreme modes of contact line dynamics as the droplet evaporates/shrinks: the constant contact angle (CCA) mode, typically ensuing in ideal cases with negligible contact angle hysteresis, and the constant contact radius or area (CCR) mode, occurring on high energy substrates in the presence of contact angle hysteresis. They then derived the relevant equations for estimation of the evaporation rate and residual mass of droplets in time, which showed good agreement with their own experimental results for a wide range of contact angles.

More recently, in 1997, upon the observation of the patterns left with the complete evaporation of a droplet of coffee, Deegan et al. [10–12] explained the formation of the so called coffee ring stain with the capillary flow originating from preferential evaporation near the pinned contact line, which has been widely acknowledged for the modeling of evaporating pure fluids and colloidal droplets. More importantly, the work revealed the interesting and non-trivial mechanisms taking place within such commonly observed phenomena, prompting a new avenue for the study of microflows and particle self-assembly via sessile droplet evaporation. Subsequently in 2002, Hu and Larson [13] derived an analytical solution to predict the evaporation rate by theoretical analysis with the Finite Element Method (FEM), which works for any initial contact angle between 0 and $\pi/2$, *i.e.*, 0° ∼90°. Yet some other analytical solutions are also proposed such as the theoretical model by Popov [14], *etc.* These analytical solutions provide an efficient way to evaluate the droplet lifetime and directly evidences the real-time strength of mass transfer.

Besides the interesting mechanisms from the mass transfer point of view, *i.e.*, water-vapor phase change, heat is removed from the droplet and/or from the substrate, resulting in a thermal effect associated evaporative cooling [15,16].
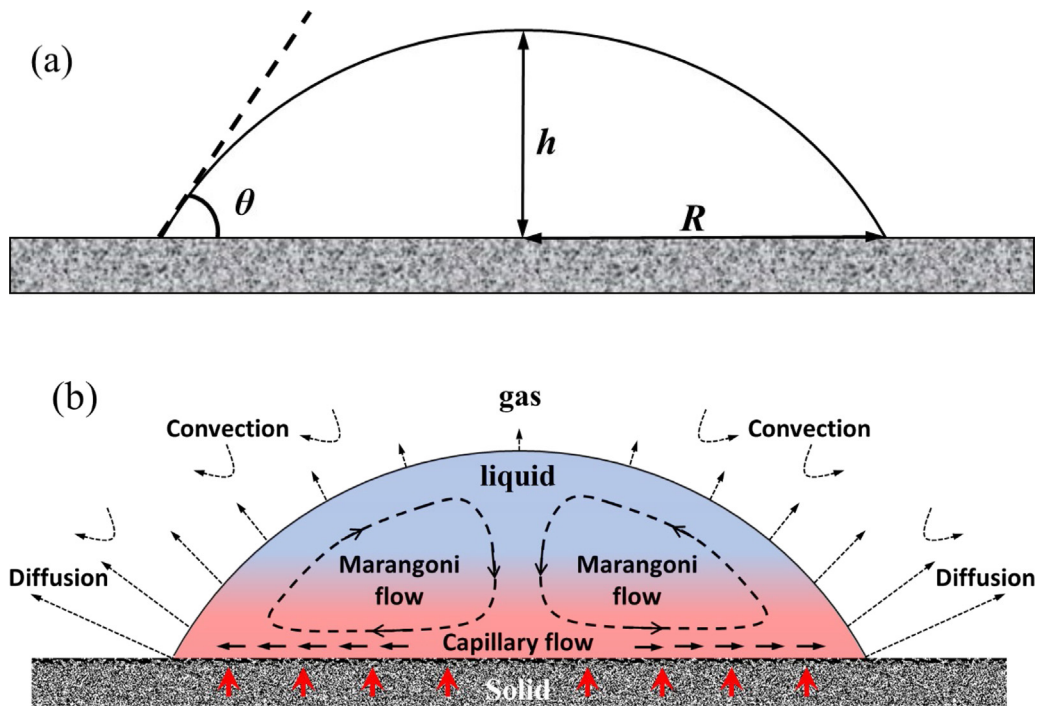
Fig. 1. (a) A sessile single-component droplet characterized by its contact angle, θ, contact radius, R, and height, h; (b) Physical mechanisms taking place with an evaporating single-component droplet sitting on a hot solid substrate ($\theta < 90°$). The droplet sketched here represents the normal cases where the surface tension of compositional liquid decreases with increasing temperatures. Red arrow: direction of heat flux within the solid surface; Dotted arrow: mass flux by diffusion and convection; Dashed arrow: direction of fluid flow induced by Marangoni effect; Solid arrow: direction of fluid flow induced by capillary effect; Gradient color within the droplet: temperature field from hot red to cold blue.

For a sessile droplet, the spherical-cap geometry, for contact angles other than 90°, gives rise to the non-uniform distribution of interfacial mass flux (which can be solved by the diffusion equations in the gas phase), leading to temperature gradients across the liquid–air interface. The temperature gradient is strong enough to induce Marangoni convection inside the droplet and in occasions flow instabilities due to small disturbances, *i.e.* the hydrothermal waves [17,18]. This is opposed to the behavior of an evaporating spherical droplet suspended in air where the diffusion of the vapor occurs homogeneously along the droplet interface [8]. Hu and Larson studied the effect of Marangoni stresses on the internal flow in an evaporating sessile droplet [19], which pointed out the reversing effect of Marangoni flow on the coffee-ring formation [20]. Sefiane et al. [18] reported the self-occurrence of hydrothermal waves in evaporating sessile droplets using infrared thermography, which is a natural consequence excited by interfacial phase change, and differs from previously reported hydrothermal waves in shallow liquid layers subjected to an imposed temperature gradient. The phenomenon is subsequently explained by Karapetsas et al. [21] using a linear stability analysis based on a lubrication-type model of an evaporating sessile droplet.

Solid surfaces influence the droplet behavior through solid–liquid interaction and by the thermal effects. Depending on the surface roughness and interfacial energy, different scenarios of droplet wetting exist [22] and the critical exponents of liquid spreading differ [23]. In the presence of evaporation, solid surfaces influence the evolution of contact angle and contact area [24–27] through the balance between the inertia of contact line motion and the surface energy barrier [28,29]. On the other hand, the substrate temperature and thermal conductivity directly influence the temperature distribution within the droplet, thus affecting the evaporation mass flux and the droplet lifetime [30–33]. Additionally, Marangoni flow may arise from the surface tension gradient due to the temperature difference across the droplet interface as represented by the internal circulatory flows indicated in Fig. 1b. Besides, at a critical contact angle, the temperature gradient and the induced Marangoni flow can change direction depending on the thermophysical properties of both the substrate and the liquid [34]. In addition to the solid surface, the mass transfer in the gas phase, which is represented by dashed and dotted arrows in the gas phase in Fig. 1(b), ensues both convectively [35] and diffusively [13], where atmospheric composition, pressure, temperature and air velocity have a strong impact [36,37].

Compared to single-component droplets, multicomponent droplets more widely exist in various domestic and industrial processes. The interplay between the different components complexes the involved physical processes and results in colorful phenomena [30]. Additions (fluids, particles, colloids, surfactants, etc.), whether volatile or not and/or miscible or not, modify the physical properties of the compositional liquid, which directly affects the physicochemical interactions with the solid surface (Section 2.1), the evaporation rate (Section 2.2), and the flow states (Section 2.3) inside the droplet.

In recent years, studies dedicated to the evaporation of multi-component droplets have seen a significant increase. New phenomena such as the phase segregation [38–40], emulsification [41,42], and nanoemulsion by ouzo effect [43–46] enrich our understanding of the colorful mechanisms with multicomponent fluid systems. We also note here that some of the previously ignored physical mechanisms such as the gravitational effect on evaporating microliter droplets have actually been reported to play a dominant role on the flow patterns within binary volatile droplets rather than the commonly recognized surface tension [47,48].

In order to provide some quantitative comparison and characterization between the different mechanisms taking place, it is necessary to introduce the different relevant dimensionless numbers that play a role. These dimensionless numbers have been frequently utilized in individual studies related to droplet evaporation, dissolution, coalescence, collision, migration, and impingement, amongst others. Table 1 summarizes these expressions, physical meanings, application scenarios, as well as in occasions approximate applicability range of values. The readers can see more detailed descriptions, applications and typical ranges of these dimensionless numbers in later sections of this manuscript. Note that some of these dimensionless numbers can be applied to liquid–gas droplet interface when the interfacial surface tension is utilized and to both the liquid and the gas phases when comparing the different mass and thermal transports.

Table 1 Dimensionless numbers for evaluating the main physical effects that control the droplet behaviors. U is the droplet velocity or the velocity of internal flow within a droplet (m/s), R is the droplet radius or characteristic length (m), v is the kinematic viscosity (m^2/s), μ is the dynamic viscosity (Pa s, or, kg/(m s)), α is the thermal diffusivity (m^2/s), γ is the liquid–air surface tension (N/m), D is the coefficient of mass diffusion (m^2/s), ρ is the liquid density (kg/m^3), g is the gravitational acceleration (m/s^2), $\dot{m}_A$ is the mass flux averaged over the droplet surface area (kg/(m^2 s)), and c is the fluid vapor concentration in humid air (kg/m^3).

In view of the diverse and continuously increasing studies, as well as the expanded understanding and novel applications of multicomponent droplets, this paper aims to provide a clear, methodical and thorough review on the so far different physical mechanisms proposed and envisaged via experimental and numerical studies, as well as to summarize the newly emerging methodologies that boost these research developments. Specifically, this paper focuses on the behaviors of multicomponent droplets induced by evaporation or mediated by the vapor field, with particular attentions to the droplet wetting and evaporation, the contact line dynamics, the evolution of interfacial mass flux, as well as the dominating mechanisms at different evaporation stages. It then summarizes the existing and newly emerging experimental techniques and available mathematical models. And it finishes providing an overlook on the challenges and opportunities in the field within the concluding remarks.

For more details on the intimate interactions at the liquid–solid interface, the readers are referred to the work by de Gennes [54], Bonn et al. [55], and Craster and Matar [56]. A more focused review on pure droplet wetting and evaporation can be found in the work by Brutin and Starov [57], by Erbil [58], and by Cazabat and Guena [59]. The readers are also referred to reviews on relevant aspects such as binary fluid mixtures [60], patterns from drying droplets [61], swimming droplets [62], surface nanobubbles and nanodroplets [63], phoretic self-propulsion [64], surfactant dynamics [65], and inkjet printing [66]. We do also recommend the reader a recent perspective review from Lohse and Zhang [67] on the physicochemical hydrodynamics of droplets out of equilibrium, which has some overlaps with the current paper while provides a more general view on the important fundamental research and relevant applications.

2. Evaporation induced droplet behaviors

2.1. Droplet spreading dynamics under complete or partial wetting

2.1.1. Pure volatile droplets

The wetting state of a sessile droplet on a solid surface depends on the binary interfacial interactions between all three phases, i.e., liquid–solid, liquid–gas and solid–gas. The wetting state can be described by the spreading parameter, $S_0 = \gamma_{SG} - \gamma_{SL} - \gamma_{LG}$, which presents the difference of surface energies per unit area between dry and wetted surfaces [54], where the subscripts S, G and L represent the solid, gas and liquid phases, respectively. On one hand, in the case of $S_0 < 0$ ($\gamma_{SG} < \gamma_{SL} + \gamma_{LG}$), the droplet will adopt a thermodynamic equilibrium state, and the force balance at the triple phase contact line (TPCL) can be macroscopically described by Young's equation [68] (without considering the intermolecular forces near the TPCL), which relates the equilibrium contact angle, θ, with the surface tension, γ, between the three phases as:

$$\gamma_{SG} = \gamma_{SL} + \gamma_{LG} \cos\theta \tag{1}$$

Eq. (1) and the force balance described by Young's equation is valid as long as the size of the droplet is below the capillary length, l_c, defined as $l_c = \sqrt{\gamma_{LG}/\rho g}$, where ρ is the liquid density and g indicates the gravitational acceleration. On the other hand, for $S_0 \geq 0$ ($\gamma_{SG} \geq \gamma_{SL} + \gamma_{LG}$), the solid–gas surface tension is strong enough to continuously drag forward the TPCL, causing the complete wetting of the liquid over the surface. In ideal cases where the liquid volume is not limited, the liquid would spread over the whole available surface and form a macroscopic film on the substrate.

At the initial stage of a liquid droplet contacting with a solid surface, the TPCL advances driven by the capillary force and is hindered by the viscous dissipation. Considering a small viscous non-volatile droplet on a completely wetting

Table 1

Dimensionless numbers for evaluating the main physical effects that control the droplet behaviors. U is the droplet velocity or the velocity of internal flow within a droplet (m/s), R is the droplet radius or characteristic length (m), v is the kinematic viscosity (m^2/s), μ is the dynamic viscosity (Pa s, or, kg/(m s)), α is the thermal diffusivity (m^2/s), γ is the liquid–air surface tension (N/m), D is the coefficient of mass diffusion (m^2/s), ρ is the liquid density (kg/m^3), g is the gravitational acceleration (m/s^2), $\dot{m}_A$ is the mass flux averaged over the droplet surface area (kg/(m^2 s)), and c is the vapor concentration in humid air (kg/m^3).

Name	Expression	Physical meaning	Note
Reynolds number	$Re = \rho UR/\mu = UR/v$	Ratio of inertial forces to viscous forces	The value is small (<0.1) for droplet wetting and evaporation, while it is considerable ($10^2 \sim 10^3$) in cases related to droplet impact and collision [49].
Capillary number	$Ca = \mu U/\gamma$	Ratio of viscous to capillary forces	Usually very small for sessile droplets, indicating the dominating effect of surface tension in droplet shape and dynamics.
Peclet number	$Pe = UR/D$	Relative strength of convective to diffusive mass transport	The value is in the range of $10 \sim 10^3$ for cases in the present review, indicating the dominating role of advection over molecular diffusion [50].
Lewis number	$Le = \alpha/D$	Ratio of thermal diffusion to mass diffusion	$10 \sim 10^2$, indicating that thermal diffusion is much faster than mass diffusion [51].
Prandtl number	$Pr = v/\alpha$	Relative strength of momentum diffusion to thermal diffusion	Thermal diffusion is typically slightly smaller than viscous transport.
Marangoni number	$Ma = \Delta\gamma R/\rho vD$	Ratio between the tangential stresses by surface tension gradient and the viscosity	The tangential stresses can be raised by thermal effect (temperature difference) Ma_{th} or solutal effect (concentration difference) Ma_s.
Rayleigh number	$Ra = gR^3\Delta\rho/\rho vD$	Ratio between buoyancy forces and viscous forces	The natural convection is considerable even for small Ra numbers.
Archimedes number, or rather, Grashof number, Gr	$Ar = gh^3\rho_0\Delta\rho/\mu^2$	Relative strength of gravitational effect to viscosity	For large $Ar \gg 1$, the gravitational effect plays a prominent role in the flow patterns within binary droplets, whereas for small $Ar \ll 1$, the gravity can be neglected, and the Marangoni effect dominates the internal flow. [48]
Sherwood number	$Sh = \dot{m}_A R/D\Delta c$	Ratio of the total mass flux to that by pure diffusion	Highly related to the strength of natural and forced convection.
Ohnesorge number	$Oh = \mu/\sqrt{\rho\gamma R}$ $= We^{\frac{1}{2}}/Re$	Ratio of viscous to surface tension effects	Utilized for the characterization of jet breakup.
Weber number	$We = \rho U^2 D/\gamma$	Relative strength of inertia to surface tension effect	For droplets impinging onto micro-structured surfaces, the wetting state transits from Cassie to Wenzel state as We increases from the scale of 10^{-1} to 10^2 [52,53].
Bond number	$Bo = \rho gR^2/\gamma$	Ratio of gravitational force to capillary force	The droplet equilibrium contact angle is related to the volume at small Bo number, while beyond a critical value, the contact angle is independent of the droplet volume.

substrate, a power law can be derived taking account of the balance between the capillary and viscous forces, known as the Tanner's law [23], which indicates the development of the contact radius, r, over time, t.

$$\frac{r(t)}{R} \sim \left(\frac{\gamma_{LG}t}{\mu R}\right)^n, \tag{2}$$

where R is the initial droplet radius, μ is the dynamic viscosity, and n is the spreading component which equals $1/10$ in this case. Tanner's law has proven to accurately describe the droplet spreading at the initial stage where the wetting radius falls below the capillary length. When the contact radius goes beyond the capillary length, the gravitational effects

start to play a role. In such cases, a different spreading component ($n = 1/7$ or $1/8$) applies to account for the gravity and dissipation within the droplet [57].

For volatile liquids, evaporation takes place along with the wetting dynamics. In the case of a partial-wetting droplet, the evaporation mass flux concentrates in the vicinity of TPCL. The continuous loss of molecules counteracts with the advancement of the TPCL and slows down the spreading. As the excess energy of the droplet dissipates, the TPCL stops advancing, then, depending on the wettability and structure of the solid surface, either the TPCL or the contact angle recedes as the liquid depletes. This phenomenon is general for a volatile droplet after its initial contact with the solid surface, which has been extensively studied experimentally and well predicted by the mathematical models based on the lubrication theory [69,70].

2.1.2. Binary volatile droplets

For mixtures composed of liquids with different vapor pressures, the component with higher vapor pressure, *i.e.*, more volatile, evaporates faster, and depletes at the region near the TPCL with the consequent generated concentration gradients. The evaporation-induced concentration gradient results in a strong surface tension gradient across the droplet interface, and induce flows over the droplet, namely the solutal Marangoni flow, characterized by the solutal Marangoni number, Ma_s. The solutal Marangoni stresses usually outweigh those induced by the temperature gradient (characterized by thermal Marangoni number, Ma_{th}). The solutal and thermal Marangoni flows as well as the effect of viscosity and gravity lead to diverse dynamics of the droplet, and in occasions deform the droplet to flattened shapes [71].

In the presence of a structured substrates, the situation is more complex and the concentration of the mixture governs the wetting regime and extent of wetting either Cassie–Baxter, partial non-wetting Wenzel, hemi-wicking or partial wetting Wenzel, as well as the geometrical shape of the droplets deposited, which eventually dictate the droplet footprint and the mechanisms of evaporation and deposits left [72,73]. For the purpose of expliciting the common physics, we focus this review on smooth substrates.

Marangoni Spreading: If the residual component has higher surface tension than the more volatile one, *i.e.* $P_a < P_b$ with $\gamma_a > \gamma_b$, upon droplet deposition and evaporation of the most volatile component, Marangoni flow originates from the area with low evaporation rate (droplet center) towards the area with high evaporation rate (near the TPCL, where liquid with high surface tension is richer). The solutal Marangoni effect (Fig. 2(a)) enhances the advancing motion of the TPCL, *i.e.* binary mixtures spread faster than both individual components [74,75]. More interestingly, complete spreading can also happen for binary mixtures composed of components that would not completely spread if deposited alone as pure fluids. In this case, the solutal Marangoni effect induced by preferential evaporation enables the droplet to overcome the energy barrier and realize complete wetting that could not have been possible for pure fluids [76], *e.g.* the phenetole–chloroform mixture.

Marangoni Contraction/Retarded Spreading: On the other hand, if the less volatile component has lower surface tension, *i.e.* $P_a < P_b$ with $\gamma_a < \gamma_b$, the surface tension near the TPCL becomes smaller than that near the droplet apex. As a result, liquid molecules are pulled towards the apex and induces Marangoni flow in the same direction. The Marangoni effect drags back the TPCL and contracts the droplet as in Fig. 2(b). In this case, droplet spreading is retarded, and the spreading rate is lower than that of both pure components [76]. Even on high surface energy substrates where complete wetting ensues for both components individually in the absence of evaporation, the binary mixture may exhibit apparent nonzero contact angle [78]. This is explained by the quasi-stationary balance between the capillary force and the increasing Marangoni stress [79]. As a result of the Marangoni contraction, the contact angle of droplets consisting of vicinal alkanediols and water may increase with the concentration of vicinal alkanediols, even though a decrease in the liquid–gas surface tension is expected [80]. Interesting phenomenon also happens for a binary-mixture droplet immersed in another liquid bulk, *e.g.* a mixture of pentanol and decanol in water [38]. Apparent deformation of such droplets and deviation from spherical cap shape is observed with a wider footprint radius and contact angles smaller than the value of an ordinary spherical cap (as shown by Fig. 12 in Ref. [38]), which is attributed to the local difference of surface tension across the liquid–liquid interface arising from the preferential dissolution of pentanol into water.

Self-rewetting fluids: Self-rewetting fluids are one type of aqueous solution whose surface tension depends non-monotonically on temperature [81]. Typical self-rewetting fluids include dilute aqueous solutions of high carbon alcohols (number of carbon atoms > 4) [82,83] such as butanol, pentanol, hexanol, *etc*. These mixtures exhibit a minimal value in the relation curve of surface tension to temperature as exemplified in Fig. 3. The minimum temperature decreases with the increase in the number of carbon atoms. In general, these alcohol aqueous solutions are the so-called negative mixture, in which alcohol is the less volatile component. In a dilute composition (self-rewetting fluids), however, aqueous solutions behave like positive mixtures, that is, alcohol composition preferentially evaporates [82]. As the liquid temperature increases, the interaction between alcohol molecules and water molecules changes. The attraction/repelling trends between molecules at the liquid–air interface directly reflect on the value of the interfacial stresses, leading to the non-monotonical variation of surface tension.

At the low temperature region (region ①), the surface tension decreases with temperature as typically occurs for pure fluids. Conversely, in the high temperature region (region ②), the surface tension increases with temperature. As a result, when a self-rewetting fluid droplet is placed on a smooth substrate with a temperature gradient [84], the droplet will move towards the cold side when the substrate temperature locates in region ①, while it moves towards the hot side when
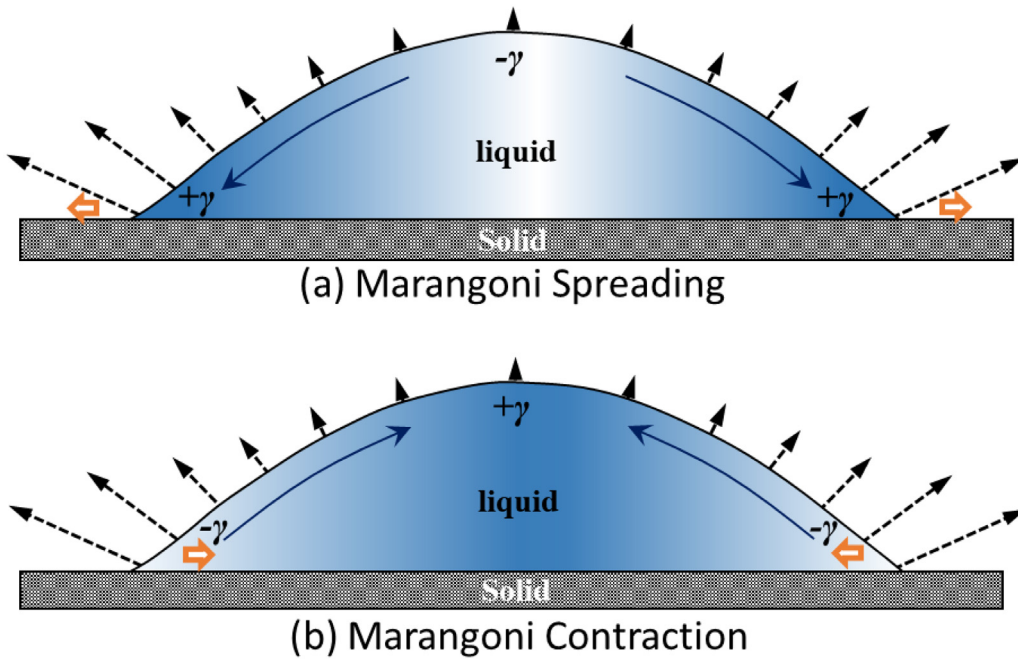
Fig. 2. (a) Spreading or (b) contraction of a multi-component droplet induced by solutal Marangoni effect due to preferential evaporation of the low surface tension component or the high surface tension component at the TPCL, respectively. The color gradient fill within the droplet qualitatively indicates the concentration of the high-surface tension component as dark blue and that of the low surface tension fluid as light blue/white. Solid arrows represent the surface tension increase, dashed arrows the evaporative flux, while hollow orange arrows represent the spreading or retraction direction of the TPCL.
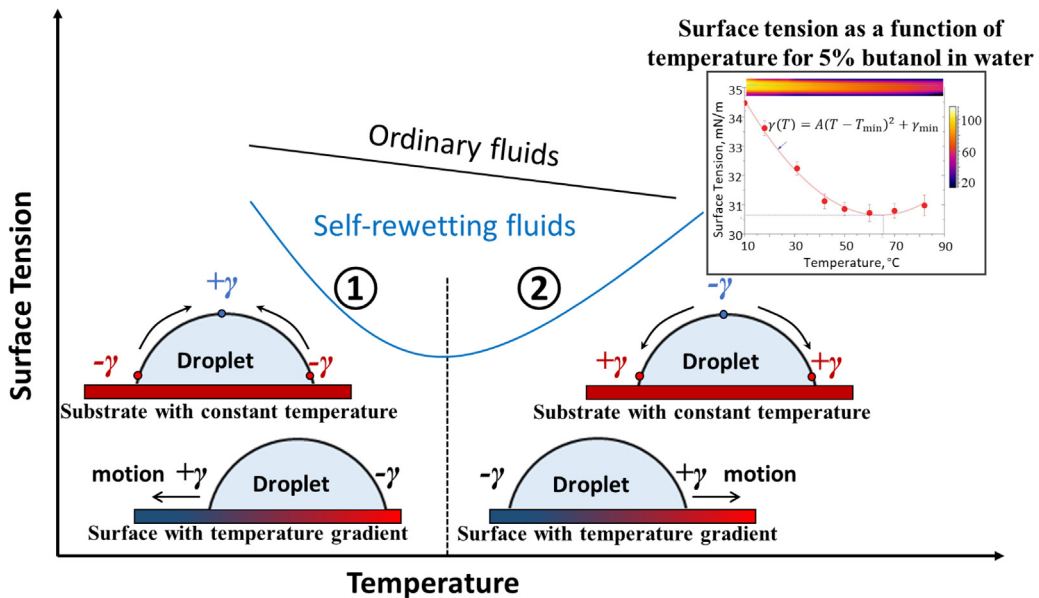
Fig. 3. Conceptual schematic of physical phenomena involved with self-rewetting fluid droplets. The blue solid line indicates the surface tension, γ, dependence of self-rewetting binary fluids on temperature while the black solid line represents that of ordinary fluids. At regions ②, the surface tension of self-rewetting fluid increase with increasing temperature. For a droplet on a surface with temperature gradient at this region, the droplet will move towards the hot side driven by the surface tension gradient. On a hot substrate with constant temperature at regions ②, a surface tension gradient rises from the droplet apex towards the edge, causing Marangoni convection in the same direction inside the droplet. (Surface tension as a function of temperature for 5% butanol aqueous solution is provided [77].)

the substrate temperature locates in region ②. Such special characteristics of self-rewetting fluids denotes its application potentials in evaporation-based thermal components such as heat pipes and thermosyphons where the coolant liquid is desired to move towards the hot spots to avoid dry-out [85–87]. The interplay between thermocapillary stresses and body forces also greatly affects the contact line movement which leads to the temporal non-monotonic dependence of the contact-line velocity. In some instances the droplet motion against the gravity is possible with designed temperature gradients [85,88]. In the presence of a heated substrate with uniform temperature, *e.g.* for a self-rewetting droplet on region ①, a surface tension gradient arises from the droplet edge to center, which tends to contract the droplet. Whereas for a self-rewetting droplet on region ②, the surface tension gradient arises from the droplet center to the edge, which tends to spread the droplet.

2.1.3. Ternary volatile droplets

By taking advantage of the interaction between capillary effect, thermal Marangoni effect and solutal Marangoni effect, phenomena with high complexity can be predicted or even designed. For example, for a three-component droplet composed of water, ethanol, and propylene glycol on a completely wetting substrate, the preferential evaporation of ethanol will result in a surface tension gradient towards the edge of the droplet and induces rapid spreading. As the ethanol depletes continuously, the subsequent evaporation of water will reverse the direction of surface tension due to the high concentration of residual propylene glycol at the TPCL, which tends to contract the droplet [89]. Such phenomenon indicates its application potentials in self-cleaning devices. The dynamics of some other ternary liquid systems can be predicted and explained based on the evolution of the mass flux and interfacial parameters in a similar way.

2.1.4. Droplets with nonvolatile components

Common liquids with nonvolatile components include surfactant solution, saline solution, colloidal suspensions, *etc.* Depending on the properties of the nonvolatile components, the droplet displays different dynamics as the concentration of the nonvolatile component changes. Regarding the spreading dynamics, the surfactant solution droplets is one representative and have been extensively studied due to its significance in many chemical processes. In this part, we focus on the spreading mechanisms of surfactant solution droplets, while in the following sections (Section 2.2 on droplet lifetime and Section 2.3 on flow patterns), the more representative saline solution droplets will be reviewed.

Surfactants are compounds which contain hydrophobic tails and hydrophilic heads [90]. Surfactants can diffuse in water or adsorb at the water–air interfaces. Due to the presence of a surfactant, the surface tension is lowered at both the liquid–gas and the liquid–solid interfaces. When dissolved in water, the surfactants can aggregate and form micelles with the hydrophilic heads contacting with the liquid bulk and the hydrophobic tails forming the core of the aggregates. The distribution of surfactants at interfaces depends on the adsorption and desorption characteristics and relates to the diffusion coefficient of the surfactant.

When depositing a surfactant solution droplet on a solid substrate, the surfactant molecules will diffuse and adsorb onto the solid interface through the TPCL, thus modifying the wetting characteristics of the solid surface [91]. Compared to pure liquid droplets governed by Tanner's law (driven by capillarity), the surfactant solution droplets indicate higher spreading rates upon contact with the solid substrate [92]. In the case of constant mass of surfactant below the critical micellar concentration (cmc), the spatial location of the surfactant leading edge follows a power law in time [93], *i.e.* $r(t) \sim t^{1/4}$, based on the numerical simulation with a lubrication type model and verified by experimental observations [94–96], where $r(t)$ denotes the position of the leading edge of a droplet in time. For those with a reservoir feed of surfactant, the spreading process scales as $r(t) \sim t^{1/2}$ [92,96] owing to the in-time supplementary of surfactant from the reservoir towards the leading edge. These power-laws reflect the dominance of Marangoni stresses in the spreading of surfactant-laden droplets over the capillary effect (where $r(t) \sim t^{1/10}$ in the case of capillary spreading of pure water droplets). Additionally, a certain type of aqueous droplet with trisiloxane-based surfactants can spread on moderately or highly hydrophobic substrates with a very small final contact angle, namely the superspreading phenomenon [97,98]. From the molecular point of view, the superspreading phenomenon is owed to the adsorption of surfactant molecules from the liquid–vapor surface onto the three phase contact line (TPCL) augmented by local bilayer formation [97]. Additionally, this must be coordinated with the rapid replenishment of liquid–vapor and solid–liquid interfaces with surfactants from the interior of the droplet, which contributes to a constant strong Marangoni flow that drives the forward moving of the leading edge.

Regarding the spreading behaviors of surfactant solution droplets, a rich number of experimental and numerical explorations have been carried out. Extensive analyses and explanations to the relevant phenomena can be approached through mathematical models based on the lubrication theory [99] and molecular dynamics (MD) simulations [100]. For a detailed overview of the surfactant-assisted spreading, the reader is referred to the review papers by Matar and Craster [56,92].

2.2. Prediction of droplet lifetime

2.2.1. Pure volatile droplets

For a sessile volatile droplet, the evaporation rate is closely related to the droplet profile. For sufficiently small droplets, the ratio of the gravitational force and capillary force is usually small, indicated by the Bond number, Bo =

$\rho g R h_0 / \gamma \ll 1$, where ρ is the fluid density, g is the gravitational constant, R is the contact-line radius, h_0 is the initial height of the droplet, γ is the air–water surface tension. In such cases, the droplet shape is governed by the surface tension, and can be regarded as a spherical cap. Based on the spherical cap assumption as well as by considering the gas phase mass transfer as a quasi-steady state diffusion process (valid for $R^2/D\, t_{\text{evp}}$, where D is the diffusivity of vapor in air and t_{evp} is the droplet evaporation time), the evaporation can be described with the Laplace equation, $\Delta c_v = 0$ (where c_v is the vapor concentration at the gas phase), by dealing the droplet as a charged conductor with an equivalent shape (a symmetrical double-convex lens comprised of two spherical caps in the full space) at constant potential. The analytical solution to this problem was derived originally by Lebedev [101] and Picknett and Bexon [9]. Later Hu and Larson [13] applied Finite Element Method (FEM) analysis to evaluate the evaporation rate of droplets with contact angles between 0° and 90°. By combining the FEM analysis results and the theoretical equation suggested by Deegan et al. [10–12], $\vec{J} \cdot \vec{n} = J_0 \left(1 - \tilde{r}^2\right)^{-\lambda}$ (where λ is a fitting parameter representing the nonuniformity of the evaporation flux on the droplet surface and $\tilde{r}$ is the dimensionless contact radius), they derived an approximate expression for the droplet evaporation rate at any contact angle between 0° and 90°, $\dot{m}(t)$= $-\pi RD(1\text{-RH})c_{v,\text{sat}}\, (0.27\theta^2 + 1.30)$, where R is the droplet contact radius, θ is the contact angle, and D is the diffusion rate of water vapor, RH is the relative humidity of the gas phase, $c_{v,\text{sat}}$ is the saturation concentration of water vapor. The expression proves to agree well with the theoretical results by electrostatic analysis [101] and with the experimental results reported previously [102]. Popov revisited the equivalent electrostatic problem, and derived a substantially simple result of the evaporation rate, $\dot{m}(t) = -\pi RD \left(c_{v,\text{sat}} - c_{v,\infty}\right) \left[\frac{\sin\theta}{1+\cos\theta} + 4\int_0^\infty \frac{1+\cosh 2\theta\tau}{\sin 2\pi\tau} \tanh\left[(\pi - \theta)\tau\right] d\tau\right]$. This analytical solution by Hu and Larson as well as the one by Popov have been frequently utilized in later studies as a theoretical contrast with the experimental results [13,101].

In the case of a flat droplet with a contact angle < 90°, the mass flux concentrates near the TPCL. In such cases, a droplet evaporating in CCR mode (pinned contact line) anticipates a shorter lifetime than that of a droplet with the same initial profile while evaporating in CCA mode (receding contact line) [17] due to the large effective area for evaporation. In the case of droplets with a contact angle > 90°, the interfacial mass flux near TPCL is suppressed due to the constraint space for vapor diffusion therein. Additionally, the evaporative cooling effect in hydrophobic and superhydrophobic cases, *i.e.*, > 90°, is more apparent due to less efficient heat supply from the substrate as a consequence of the extra heat transfer resistance imposed by the droplet thickness, which may further lower the evaporation rate [27].

The substrate conductivity, which directly affects the heat transfer process, also plays a decisive role in the droplet lifetime. By taking account of the Newton's law of cooling and the vapor buoyancy in the atmosphere, Hu and Larson's equation for droplet evaporation rate can be improved by relating the variation of the saturation vapor concentration with the temporal interfacial temperature [30,32], which provides a better prediction of the real-time evaporation rate. Detailed investigations on the evaporation rate and lifetime of pure liquid droplets have been massive. Since the main focus of this review is on multicomponent droplets, the readers are referred to the review papers by Brutin and Starov [57] and by Erbil [58] for more details of the lifetime prediction and the relevant factors for single component droplets.

2.2.2. Binary volatile droplets

When it comes to binary volatile droplets, the most volatile component evaporates first. This leads to the non-constant or non-monotonic decrease of the evaporation rate, different from that of pure volatile droplets [103,104]. In such cases an apparent decrease in the evaporation rate is highlighted where the typical evolution curve of droplet volume with time indicates an obvious concave trend [105,106]. The average evaporation rate is between the evaporation rates of two individual components. Specifically, the initial evaporation rate is close to that of the more volatile component, while the evaporation rate at the terminal stage is close to that of the less volatile component. The preferential evaporation of more volatile components can be strong enough to induce volatile solutal Marangoni effect and the break of axisymmetric flow geometry as described later in Section 2.3.2 on the flow patterns of binary droplets.

When looking into the droplet dynamics, *e.g.* the evolution of contact angle and contact radius, it greatly depends on the initial composition of the binary mixture and on the physicochemical properties of the solid surface. On a smooth hydrophobic substrate, *e.g.* PTFE [103,104,107,108], silicon wafer coated with PDMS [106] or gold surfaces modified with alkanethiolate self-assembled monolayers [105], the evaporation of a binary volatile droplet, *e.g.* ethanol and water, can be divided into three distinct modes as in Fig. 4. Upon contact with the substrate, the more volatile component, *e.g.* ethanol, starts to evaporate. The large evaporation rate of ethanol causes the decrease of droplet height and contact radius induced by the liquid depletion taking place near the TPCL and with a slight variation of the contact angle (Fig. 4a). Additionally, at the initial stage, the supplement of ethanol from the droplet bulk to the surface is efficient, therefore, the interfacial composition and the surface tension do not change considerably in time, *i.e.*, good mixing. As ethanol gradually depletes, the water concentration at the droplet surface increases, and so does the surface tension. Consequently, the contact angle increases with continuously shrinking contact area (Fig. 4b). As evaporation goes on, the composition of the droplet tends to that of the least volatile component resembling a single component droplet. In the specific case of an ethanol–water droplet, the evaporation behavior is close to that of a pure water droplet at the final stage, shown as, the contact angle and contact area decrease simultaneously until the whole droplet vanishes in the mixed mode as represented by Fig. 4c. On smooth hydrophilic substrates, non-monotonic contact line motions are observed along with the evaporation of binary mixture droplets (*e.g.* on a thin gold film by Jeong et al. [109]). Specifically, the droplet kinetics can be divided into three stages: (I) the spreading stage, where the contact line spreads for tens of seconds, (II) the rapid sliding stage, where the
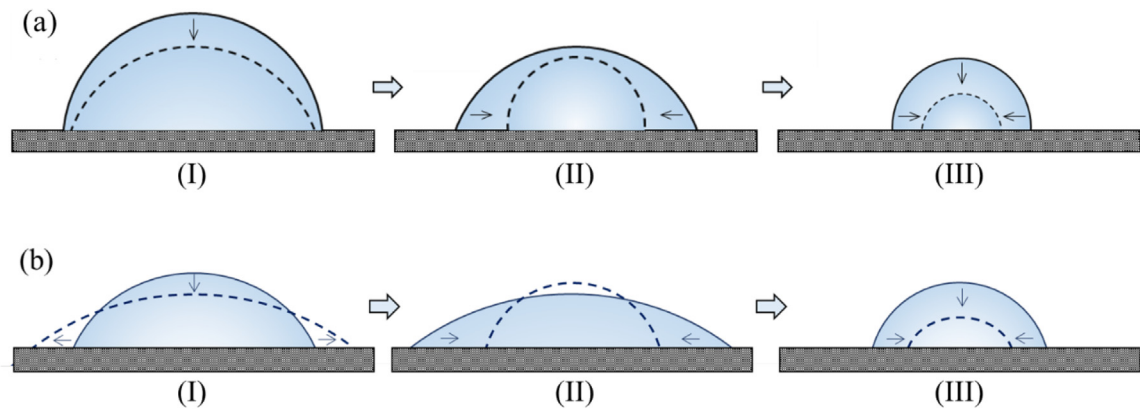
Fig. 4. (a) Dynamics of an evaporating binary volatile droplet on a smooth hydrophobic substrate, *e.g.* PTFE [103,104,107,108], silicon wafer coated with PDMS [106] or gold surfaces modified with alkanethiolate self-assembled monolayers [105]: (I) decreasing contact angle with slightly shrinking contact area; (II) increasing contact angle with shrinking contact area; (III) decreasing contact angle with shrinking contact area as in the mixed mode. (b) Dynamics of an evaporating binary volatile droplet on a smooth hydrophilic substrate, *e.g.* thin gold film [109]: (I) spreading with continuous advancing contact line; (II) rapidly receding contact line with increasing contact angle; (III) moderate sliding with decreasing contact radius and contact angle.

contact radius rapidly decreases, and the contact angle continues to increase until it reaches its maximum value, (III) the moderate sliding stage, which is nearly identical to the depinning stage of a pure water droplet, where the contact radius and contact angle decrease until the end of the droplet's lifetime. Similar evaporation dynamics of binary volatile droplets has also been reported in the study of Williams et al. [110] on a smooth and superhydrophilic substrate, which is well explained by the interaction between capillary flow, solutal Marangoni flow and thermal Marangoni flow with a lubrication-type model as introduced in later sections.

On an inclined aluminum substrate covered with PTFE tape and with controlled temperature, it shows that the ethanol–water mixture droplet remains pinned at the advancing side during evaporation, while contracts at the receding side [111]. The evaporation dynamics can be divided into (I) an early stage when the advancing and the receding (front and rear) contact angles increase, (II) an intermediate stage when the droplet contact angles exhibit a slow decrease and (III) a late stage when both contact angles decrease rapidly as the small residual droplet undergoes a rapid unsteady contraction. On the inclined substrate, the tilted droplet shape causes the formation of water-rich cold regions near the advancing contact line as well as hot and rapidly evaporating ethanol cell near the receding contact line. The preferential evaporation along with the component segregation induce complex convection dynamics leading to oscillatory thermo-solutal convection cells and thermal pulsations [111].

The evaporation rate and droplet behavior also depend on the relative humidity of the ambient [107]. Due to liquid–vapor phase change, the effect of evaporative cooling will cause the temperature decrease at the droplet interface. In a moist atmosphere, adsorption/absorption or condensation of water vapor may take place during the evaporation of volatile organic solvent droplets [112]. This latter study and an earlier one reported by Fukatani et al. [113] point out to the ubiquitousness of binary-mixture droplets where a pure single component droplet transitions into a binary mixture upon exposure to the surroundings with certain degree of humidity. During organic solvent droplet evaporation, in the presence of low relative humidity, the surrounding water vapor may adsorb/absorb onto the droplet interface changing the composition of the pure droplet, while in the presence of high humidity, water vapor may also condense onto the surface as the droplet interface temperature becomes lower than that of the dew point [113]. Thereafter, as ethanol continues to deplete, a droplet of pure water remains at the final stage as evidenced by its high final contact angle seemingly to the equilibrium contact angle of a water droplet on the studied surface [106,112]. The specific composition of the binary droplet at different stages can be characterized with advanced experimental techniques, such as confocal microscopy, gas injection chromatography or refractometer, which will be introduced later in Section 4.

Empirical expressions for the evaporation rate of binary volatile droplets based on the single-component models have been recently developed [112,114]. Such empirical formulas account for the physical properties of the binary mixtures, able to track the general evolution of droplet volume and average concentration. Nevertheless, other detailed information such as the spatial distribution of interfacial mass flux and heat flux cannot be predicted to date, which requires a full solution with a well-established numerical model.

2.2.3. Droplets with nonvolatile components

For a sessile saline solution droplet, the existence of non-volatile ions modifies the vapor pressure at the liquid–air interface and affects the molecule–molecule interactions at the liquid–solid interface. Experiments with sessile saline solution droplets indicate that a small amount of salt addition may contribute to the pinning of the TPCL [115,116]. On
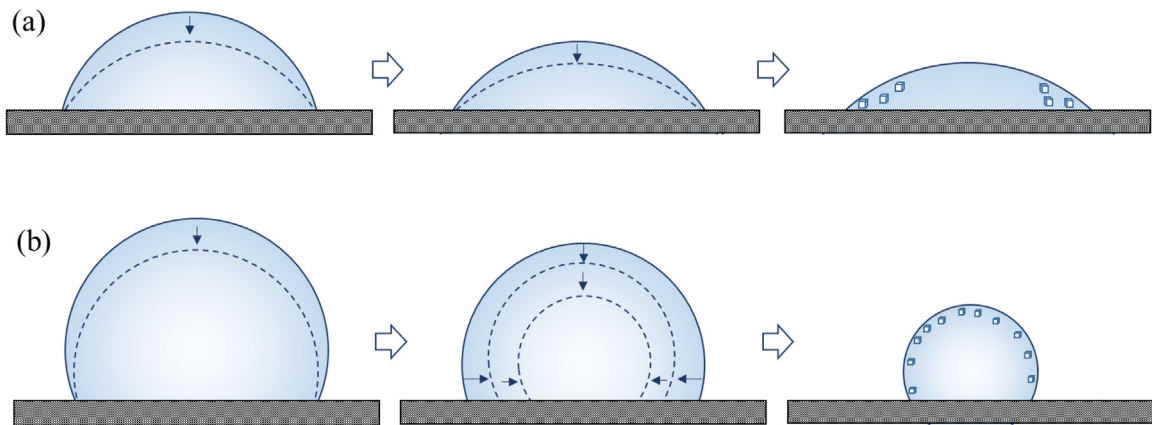
Fig. 5. Profile evolution of a saline solution droplet before the deposition of salt crystals on (a) a hydrophilic glass substrate where the contact line remains pinned with continuously decreasing contact angle, *i.e.*, CCR mode. As the salt concentration reaches a critical value, salt crystals form starting from the contact line region [115]. (b) On a smooth hydrophobic silicon wafer, a short CCR mode ensues at the initial stage, then the contact line recedes with gradually increasing contact angle resulting from the enlarged surface tension brought by increasing salt concentration [117]. Note that in the case of (b) there is no crystallization and pinning of the contact line during the first 2 frames, *i.e.*, concentration below the critical concentration, and the contact lines recedes in the absence of stick–slip motion.

hydrophilic glass substrates (Fig. 5(a)), the droplet evaporates in a CCR mode with pinned TPCL throughout the droplet lifetime. On smooth hydrophobic silicon wafer and poly plate (Fig. 5(b)), the droplet experiences a CCR mode during the initial period, then the TPCL starts to recede, and the contact angle increases gradually until the salt precipitates. The increase in the contact angle is attributed to the increase of surface tension induced by increasing salt concentration [117]. During evaporation, the droplet reaches a supersaturation state at first as water depletes. Once the ratio of supersaturation reaches a critical value, crystallization takes place [118,119]. The formation of salt crystal and its final structures depend on the property of the salt crystal [119,120], the surface wettability [118] and the ambient humidity [121]. On a hydrophilic substrate, the existence of the precursor film may lead to the formation of crystal in front of the TPCL, and the spreading ratio of the crystal structure depends on the physical properties of the dissolved salt. For example, when a sodium sulfate solution droplet evaporates on a hydrophilic glass, a dendritic structure stretches out in front of the TPCL. While for a sodium chloride droplet on a hydrophilic surface, the spreading is much slighter [118]. On a hydrophobic substrate, the crystallization is constraint by the droplet edge, and no apparent spreading is observed since the TPCL is not anchored on the hydrophobic surface.

Environmental conditions including temperature, ambient pressure and humidity also affect the evaporation rate and the deposition structure. At high-humidity conditions, the evaporation rate is low, and the resulted capillary drift towards the TPCL is weak. As a result, smoother and larger crystal structures appear [121].

The concentration field of low-vapor-pressure solute within ideal spherical droplets has been analytically solved [122–124]. Results indicate that large concentration gradients in the radial direction arise when the evaporation rate is high. Researchers [125] have also reported an enhancement in the evaporation rate for droplets with some specific ionic inclusions when compared to that of pure water droplets, which is owed to the strong convection induced by buoyancy and solutal Marangoni stresses. Such phenomenon depends on the chemical kinetics and thermodynamics of hydration of the ionic species in polar fluids, and is more apparent for salts with high solubility such as $Cu(NO_3)_2$ and NaI.

For some other hygroscopic salts such as $LiCl$, $LiBr$, $CaCl_2$, *etc.*, the water vapor pressure at the droplet surface is significantly lowered owing to the strong adhesion between the dissolved ions and the water molecules as well as the hydration effect [126–128]. In such cases, vapor absorption takes place in humid environments and the droplet volume increases, as indicated by Fig. 6. This is in contrast to all the cases reported earlier where the droplet volume decreases in time as a consequence of evaporation. Only at extremely low humidity, evaporation happens, but at a very small evaporation rate. Additionally, as the evaporation process goes on, the ion–water interaction and hydration effect enhances due to the increase of salt concentration, which further reduces the water vapor pressure at the droplet surface and terminates the evaporation at later stages [129,130].

2.3. Flow patterns

2.3.1. Pure volatile droplets

For an evaporating pure liquid droplet on hydrophilic substrates, the interfacial mass flux reaches the maximum at the TPCL. On one hand, the large mass flux near the contact line causes great heat loss and tends to cool down the droplet. On the other hand, the heat loss at the droplet interface is compensated by the heat supply from the substrate, and the efficiency of heat supply increases as the droplet height decreases from the apex to the thinning edge. As a joint result of
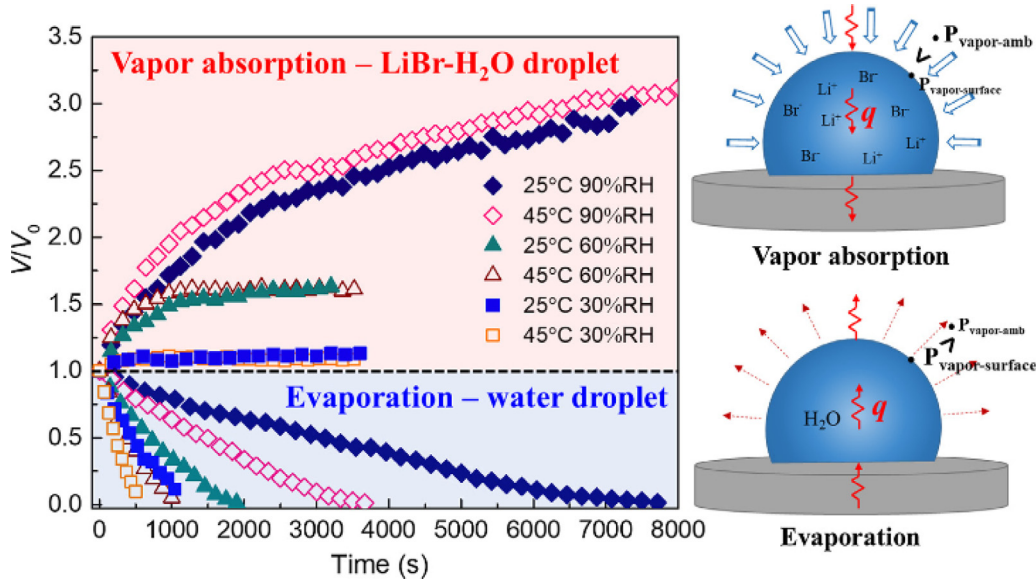
Fig. 6. Evolution of non-dimensional droplet volume with respect to the original volume, V/V_0, along with time, $t(s)$. For LiBr-H_2O droplets, vapor absorption takes place and the droplet volume increases, in contrast to the decreasing volume of pure water droplets due to evaporation [127].
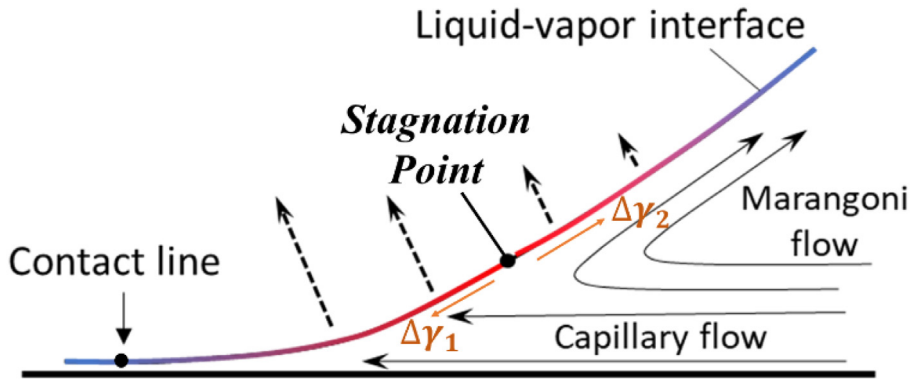

Fig. 7. Schematics of the physical processes near the contact line of an evaporating pure liquid droplet. As a joint result of evaporative cooling and heat supply from the substrate, a local temperature vertex exists at the liquid–air interface near the contact line. The formed non-monotonous surface tension gradient leads to opposite thermal Marangoni effect and forms a stagnation point as experimentally verified in Ref. [131]. (The color of the droplet interface indicates the interfacial temperature where red presents high temperature and blue indicates low temperature.)

the varying evaporation mass flux and the non-uniform heat supply, a non-monotonous temperature gradient arises at the liquid–air interface with the highest interfacial temperature existing at a position higher than the TPCL as indicated in Fig. 7. The temperature gradient induces surface tension gradients in opposite directions, resulting in a stagnation point in the flow field at the droplet interface near TPCL [131,132].

The distance between the contact line and the stagnation point depends on the thickness of the adsorbed film and on the profile of the liquid film near the contact line. In the work by Xu and Luo [131], the interfacial temperature can be estimated from the balance of evaporation heat flux and the heat supply from the substrate. The position of the stagnation point can be then derived mathematically by the vertex analysis of the temperature equation, expressed as, $x_0 = \sqrt{(2\lambda/(2-\lambda))\,h_0 R_0}$, where λ describes the non-uniformity of the interfacial mass flux, $\lambda = (\pi - 2\theta)/(2\pi - 2\theta)$ [10], h_0 is the thickness of adsorbed film and R_0 is the base radius of the droplet. For a water droplet with a base radius of 2 mm and an initial contact angle of $10°$ on a glass slide, the distance between the stagnation point and the contact line in the droplet is observed to be less than 17 μm. This result coincides with the analytical result by the above-mentioned expression.

The model proposed by Xu and Luo is based on the assumption of a constant substrate temperature. Later Ristenpart et al. [34] reported that the thermal conductivity of both the substrate and the liquid plays a crucial role on the thermal Marangoni convection within the droplet. According to their study by asymptotic analysis, if the substrate conductivity

k_S is at least a factor of 2 greater than the liquid conductivity k_L (*i.e.*, $k_R = k_S/k_L > 2$), energy could be readily supplied to the contact line region, so the droplet interface is able to maintain a comparatively high temperature despite the energy lost to evaporation. In this situation the conduction through the droplet is dominant, and the droplet is warmest near the contact line. Consequently, the Marangoni flow is directed radially outward along the substrate. For $k_R < 1.45$, energy is not readily available for substrates with low thermal conductivities. In this case, energy is extracted from the droplet itself and consequently the edge of the droplet is coldest. As a result, the circulation direction is reversed, *i.e.*, radially inward along the substrate. For $1.45 < k_R < 2$, the direction of the temperature gradient and the resulting flow depend on the contact angle θ_c. These predictions are further corroborated experimentally using organic liquids on insulating substrates [34].

For a typical water droplet on a hydrophilic glass substrate dominated by the capillary effect, a radially outward flow is observed at the droplet base near the liquid–solid interface. The magnitude of the velocities increases along the droplet radius and reaches the peak at a position close to the TPCL. In the time scale, the velocity of the outward flow increases and reaches the peak as the droplet dries out in the case of pinned TPCL, which has been coined as the "rush hour" and leads to order-to-disorder transition during colloidal particle deposition [133]. The temporal variation of the velocity magnitude can be explained by the mass conservation within the droplet to compensate for the mass loss at the droplet edge [10,13,134].

2.3.2. Binary volatile droplets

For binary volatile droplets, the flow patterns are more complex due to the spatiotemporal variation of the liquid composition within evaporating droplets. On the one hand, the thermal instability is found to increase with the ethanol concentration in an ethanol–water droplet as the gradient of surface tension with temperature for ethanol is much higher than that of water [135]. On the other hand, the concentration gradient induces strong solutal Marangoni flow, which usually overcomes that induced by the thermal effect, *i.e.*, $Ma_s > Ma_{th}$. The solutal Marangoni stresses cause strong convection within the droplet, and can be strong enough to break the axial symmetry of the flow inside [136]. Experiments carried out via μ-PIV have revealed three distinct stages during the evaporation of a representative ethanol–water droplet (Fig. 8a) [137,138]. μ-PIV (micro-Particle Image Velocimetry) is an experimental technique able to track the position of tracing particles and hence extract the velocity of the flow inside single-phase, multi-phase and evaporating droplets (see Section 4 for details of this technique). At the first stage, multiple vortices appear near the liquid–solid interface driven by the rapid diffusion of ethanol from the bulk to the liquid–gas interface as a consequence of the preferential evaporation of ethanol, which does not occur homogeneously. At the same time, surface tension gradients at the liquid–gas interface are generated and the lack or breakage of axial symmetry is evident. A transition stage follows as the ethanol gradually depletes. In this stage, the vorticity decays exponentially with time, accompanied by a migration of the remaining vorticity towards the outer edge of the drop. A remarkable spike appears in the radial velocity just before the flow settles down to that of a pure water drop. The exponential decay in vorticity can be explained by the ethanol diffusion from the bulk to the interface, while the spike is associated with the formation of a single toroidal vortex. At the final stage, the flow patterns are close to that of a pure water droplet, shown as a radial outwards flow where the radial velocity increases towards the contact line. Moreover, a dramatic rise in the radial velocity is observed towards the end of the droplet lifetime, which compensates the great mass loss near the TPCL in a similar fashion to the "rush hour" peak on the velocity reported for a pure fluid by Marin et al. [107]. Similar vortices and the final settle-down have also been observed in other type of binary volatile droplets, *i.e.* toluene and ethanol mixtures [139].

In addition, the concentration gradient arising from non-uniform evaporation in the case of a binary volatile droplet will also lead to a liquid density gradient with the consequent induced gravitational flow within the droplet. For microliter droplets with contact radius smaller than the capillary length, l_c, the conventional view is that the surface tension dominates the droplet morphology/shape as well as the internal flow rather than the gravity. However, the experiments by Edwards et al. [47] and Li et al. [48] showed surprisingly different results. Edward et al. utilized the rotating optical coherence tomography to explore the interaction between gravity and surface tension. By rotating the droplet upside down, the direction of density gradient inverses while the direction of surface tension gradient remains the same. It was found that the direction of the internal flow is in accordance with the direction of the density gradient rather than with the surface tension gradient (Fig. 8c). Similar results were also observed by Li et al. with μ-PIV techniques by changing the composition of the binary droplet (combination of components with different density, surface tension and volatility) (Fig. 8b). It is concluded that, the magnitude of gravitational effect depends on the droplet height, the viscosity difference and the density difference between the two components, which can be quantitatively evaluated by the Archimedes number $Ar = gh^3\rho_0\Delta\rho/\mu^2$ (or rather, Grashof number, Gr), where h is the height of the droplet, ρ_0 denotes the density of the reference state, $\Delta\rho$ is the density difference between the individual components, and μ is the dynamic viscosity of the binary mixture. For large $Ar \gg 1$, the gravitational effect plays a prominent role in the flow patterns within binary droplets, whereas for small $Ar \ll 1$, the gravity can be neglected, and the Marangoni effect dominates the internal flow [48].

Besides the experimental work reported above, paramount important contributions have been reported numerically. Diddens et al. [140] developed a quasi-stationary model for explicitly describing the interaction between the Marangoni flow and Rayleigh flow for both sessile and pedant binary droplets (glycerol–water), and derived the phase diagrams of Marangoni number, Ma, and Rayleigh number, Ra, for droplets with a wide range of contact angles. We briefly remind the
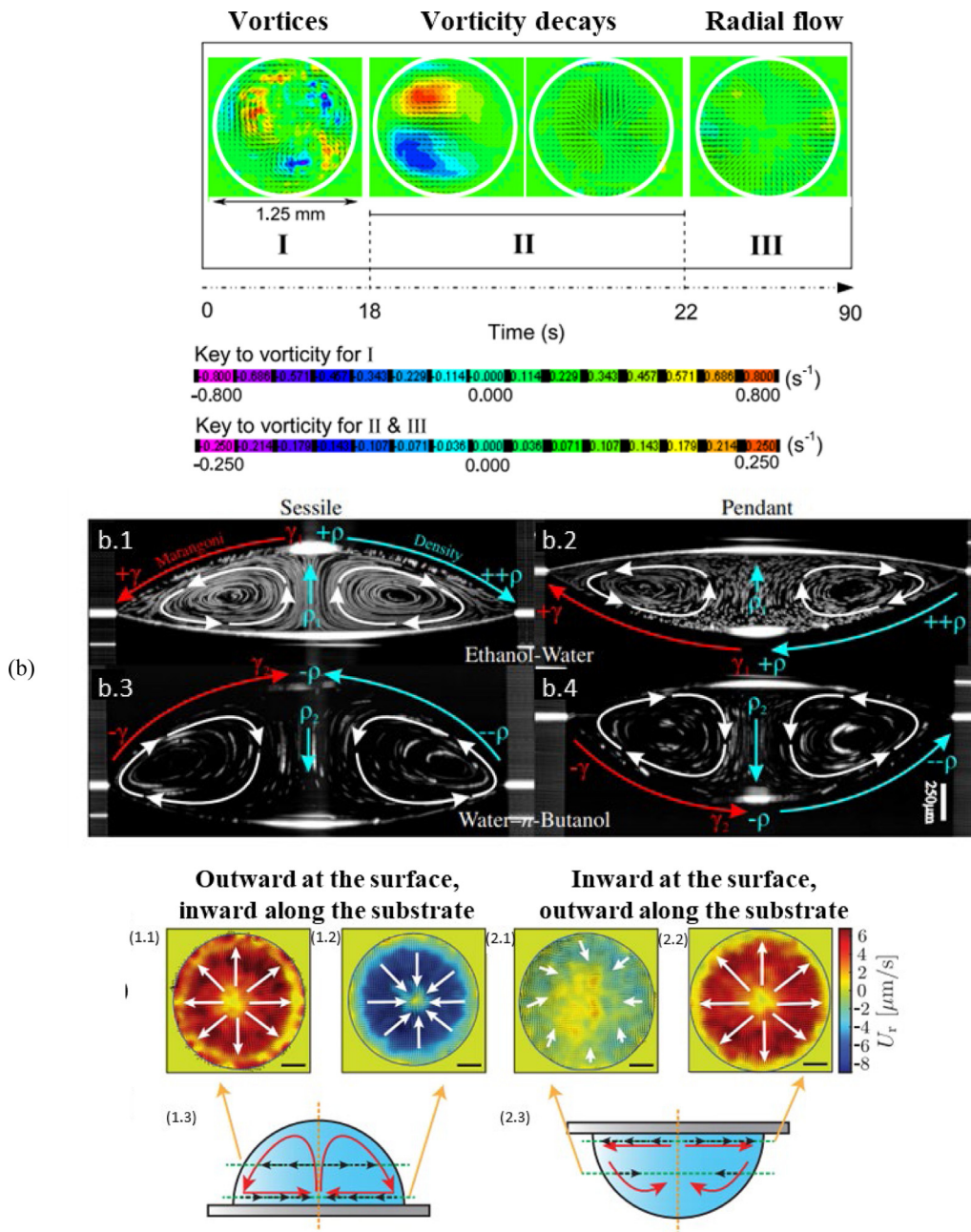
Fig. 8. Flow patterns by μ-PIV techniques. (a) Time evolution of flow patterns at the bottom of a sessile ethanol–water droplet (5:95 wt%, 0.12 $\pm 0.03\mu$L) [137]; (b) Time-averaged cross-section images of sessile and pendant 2 μL droplets over 30 s of stage II evaporation as described in [47]: (b.1, b.2) ethanol–water; (b.3, b.4) water-n-butanol; (c) Flow patterns at different cross-sections (near the droplet surface and near the substrate surface) of sessile and pendant water–glycerol droplets (50:50 wt%, 0.18 $\pm 0.03\mu$L) [48].

reader that Ma establishes the ratio between tangential stresses generated by surface tension gradient (either thermal or solutal) and viscous stresses while Ra relates the ratio between buoyancy forces and viscous forces. Further definitions of the different dimensionless typically utilized in these investigations can be found in Table 1 in the Introduction section. Both on a hydrophilic and on a hydrophobic substrate (Figs. 9a and 9b), five different flow patterns are found depending on the relative strength of the Marangoni effect and the gravitational effect (natural convection). If one of the mechanisms significantly outweighs the other (the Marangoni number or Rayleigh number is much larger than the other) (type 1 and type 2), this mechanism will dominate the flow patterns of the entire droplet, and a single vortex forms inside the droplet. When the strength of two mechanisms are comparable while the resulted flows are in different direction (type 3 and type

4), two vortices form, one in the droplet bulk driven by natural convection (gravity) and a counter-rotating vortex near the droplet interface driven by Marangoni effect. When the two comparable effects act in the same direction, it is hard to distinguish the particular cause and only one vortex exists within the droplet. The fifth type of flow pattern forms as a particular regime of the fourth type, in which case the direction of Marangoni flow reverses as a result of the natural convection inside, shown again as two vortices. This is because the bulk flow driven by natural convection distorts the concentration field inside the droplet and therefore the diffusion dynamics. The disturbance can eventually change the concentration distribution at the droplet interface and reverses the Marangoni flow there.

Due to the existence of the density gradient, Rayleigh–Taylor instability may arise from the phase separation in an evaporating silicone-oil-seeded 1,2-hexanediol-water droplet (See the embedded image showing Rayleigh–Taylor instability in Fig. 12) [141]. This phenomenon provides another example showing that Rayleigh convection can overcome Marangoni effects to control the flow structure in a milli-sized droplet with Bo < 1.

Interesting phenomena of fluid dynamics may take place as a result of the thermal effect and the complex flows inside the droplet. For a binary droplet with partial miscible liquids, phase separation or demixing may happen as the volatile solvent evaporates. Sadafi et al. [142] developed a simple model for this system taking account of the solutal and thermal effect, and attributed the demixing phenomena to the considerable temperature reduction (∼20 °C) caused by evaporative cooling along with the change of composition. Yet the phase separation/segregation phenomena may also happen for binary droplets with fully miscible liquids. Experiments by Li et al. [39] demonstrate a clear segregation between water and 1,2-hexanediol as water evaporates preferentially near the TPCL of the droplet. Specifically, the evaporation of this types of mixtures can be classified into five phases according to the evolution of the internal flow patterns elucidated via μ-PIV (Fig. 10). In the early phase, there is a predominant outward radial flow, resulting in a constant low vorticity. After destaining of the particles introduced for imaging, there are some small vortices appearing near the droplet rim due to the receding contact line. When segregation starts, the vorticity sharply increases due to a series of vortices forming in the nucleated microdroplets of 1,2-hexanediol. During the coalescence of the growing nucleated microdroplets, small vortices merge, forming larger ones. When the growing microdroplets reach the area where floating particles reside, the particles sediment to the bottom. Finally, the flow becomes irregular and then vanishes at the end of the evaporation process [39]. Based on the analysis of internal flows, the phase segregation is attributed to the fast preferential evaporation of water at the droplet rim while the Marangoni flow is not strong enough to lead to an efficient liquid mixing. The experimental observation is further verified with a numerical model. Similar phenomena of phase segregation is also revealed in the work of Kim and Stone [40] with different liquid compositions and by selectively dissolving materials.

2.3.3. Ternary volatile droplets

For a ternary droplet composed of ethanol, water and a small amount of surfactant, the solutal Marangoni stress by ethanol–water concentration gradient and the surfactant-driven Marangoni stress interact with each other. For a sessile ethanol–water droplet (35:65 wt%, 0.60 ±0.07 μL) with 0.05 wt% sodium dodecyl sulfate (SDS) (Fig. 11) [143], multiple vortices appear at the first stage driven by the solutal Marangoni flow arising from the fast depletion of ethanol, which are imaged at the bottom of the droplet, *i.e.*, near the solid–liquid interface in the x-y plane. We note that these vortices have been found to be three dimensional [140], which cannot be strictly judged by the μ-PIV technique applied by the authors [39]. The vortices decay after a short period, followed by regular flow circulations within the droplet. Specifically, the non-uniform evaporation mass flux across the droplet interface causes the quick depletion of ethanol near the TPCL. The concentration gradient of ethanol then induces a surface tension gradient, resulting in an outward flow near the liquid–air interface and an inward radial flow along the droplet base. As evaporation goes on, surfactant accumulates at the TPCL, and the concentration of ethanol decreases. The concentration gradient of surfactant drives an internal flow along the liquid–air interface and an outward radial flow along the droplet base. The surfactant-driven effect gradually outweighs the effect of ethanol distribution, thus the circulation direction of the internal flow inverses. As the surfactant reaches its critical saturation concentration, a typical outward radial flow forms, similar to that occurring within pure liquid droplets, until the droplet fully vanishes.

Another interesting ternary system is the so-called Ouzo droplet. The Ouzo effect is a phenomenon arising from a ternary mixture of two volatile liquids and a less volatile soluble oil. In a typical sessile Ouzo droplet composed of ethanol, water and anise oil, the preferential evaporation of ethanol causes the nucleation of oil microdroplets below a specific ethanol concentration [44,45]. Depending on the dominating physical process, the evaporation of an Ouzo droplet can be characterized with several different phases. For a partial wetting droplet on a hydrophilic substrate [44], at the first phase, ethanol inside the droplet evaporates preferentially near the droplet edge. As the concentration of ethanol decreases below a critical value, oil microdroplets nucleate near the TPCL. With evaporation going on, oil microdroplets nucleate quickly throughout the whole drop, *i.e.*, also within the bulk, leading to a characteristic milky color of the droplet in phase II. As ethanol depletes, the droplet becomes clear again, which is actually a water droplet sitting on an oil ring in phase III. At the final stage, water evaporates gradually and leaves a tiny spherical cap-shaped oil droplet behind during phase IV.

Things are somewhat different when it comes to droplets on a hydrophobic substrate. Specifically, on a superamphiphobic surface (both superhydrophobic and superoleophobic) [144], evaporation takes place preferentially at the top of the droplet. The nucleation happens firstly at the droplet top, and gradually spreads all over the droplet, and forms an oil shell wrapping the drop, which is different from the oil ring near TPCL in the hydrophilic cases. Along with the nucleation of oil microdroplets, the preferential evaporation of ethanol induces solutal Marangoni flow, which transports the microdroplets throughout the whole droplet and contributes to a more homogeneous concentration field and temperature field.
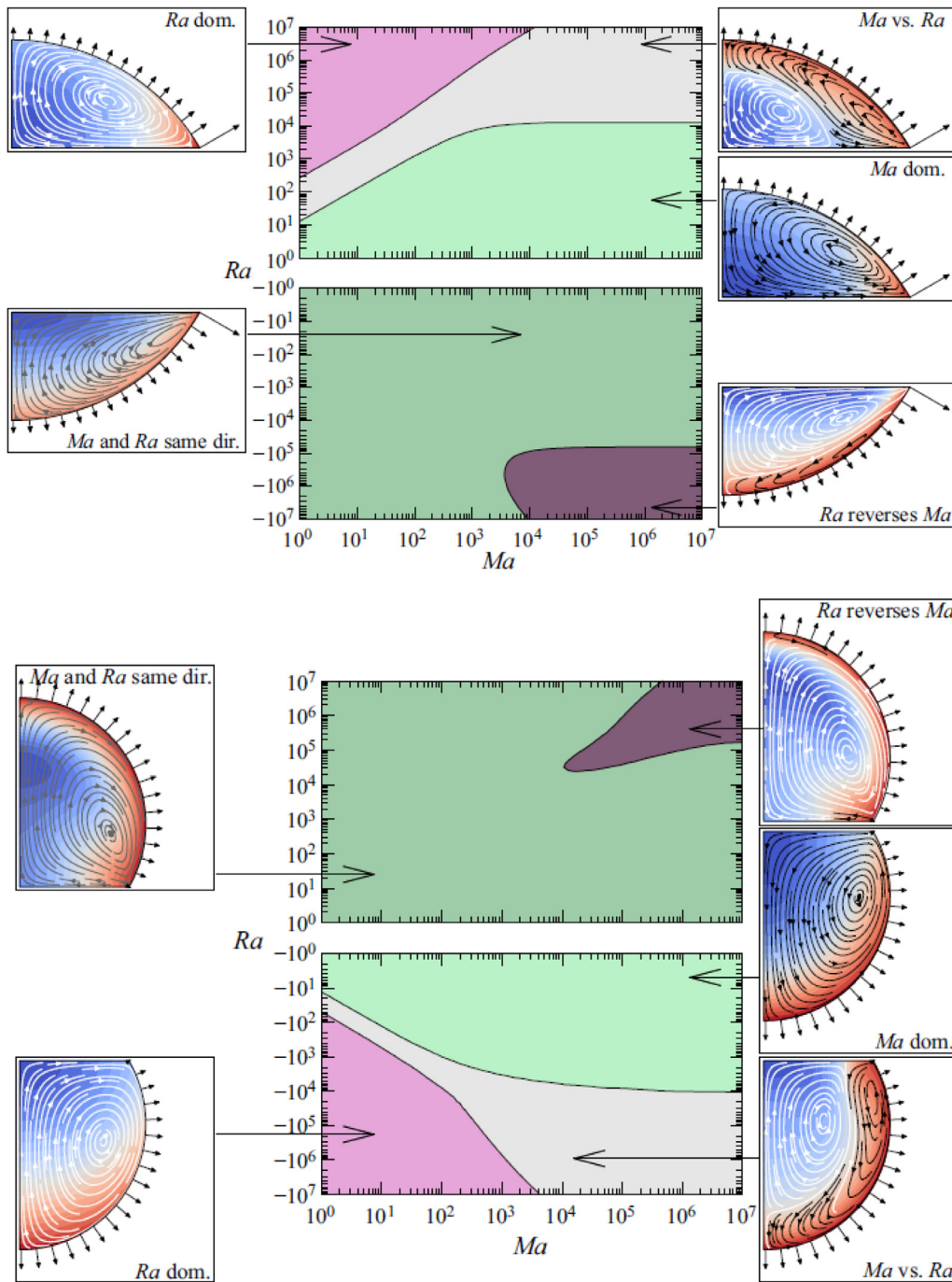
Fig. 9. Qualitative flow types as functions of the Marangoni number Ma and the Rayleigh number Ra (a) for a small contact angle $\theta = 60°$ [140]; (b) for a high contact angle $\theta = 120°$ [140].

We can see that the interaction between the capillary effect, the Marangoni effect and the gravitational effect decides the internal flow pattern of an evaporating multicomponent droplet. Additionally, these effects depend greatly on the distribution of interfacial mass flux and the motion of the TPCL. By tuning the interfacial mass fluxes and the TPCL kinematics, we are able to control the flow patterns and thus the deposition geometry from a drying droplet. For example, Li et al. [145] control the mass flux distribution by hindering the evaporation at the rim of a droplet with the non-volatile oil meniscus, which greatly weakens the outward capillary flow and thus suppresses the coffee-ring effect. Besides, with the addition of surfactants, the surface energies can be tuned, which changes the dynamics of the TPCL, thus controls
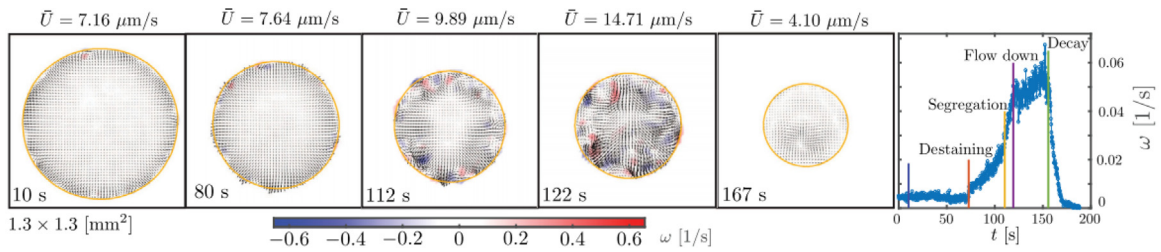
Fig. 10. Flow field by μ-PIV indicates the different stages during the evaporation of a 1,2-hexanediol-water droplet with phase segregation [39].
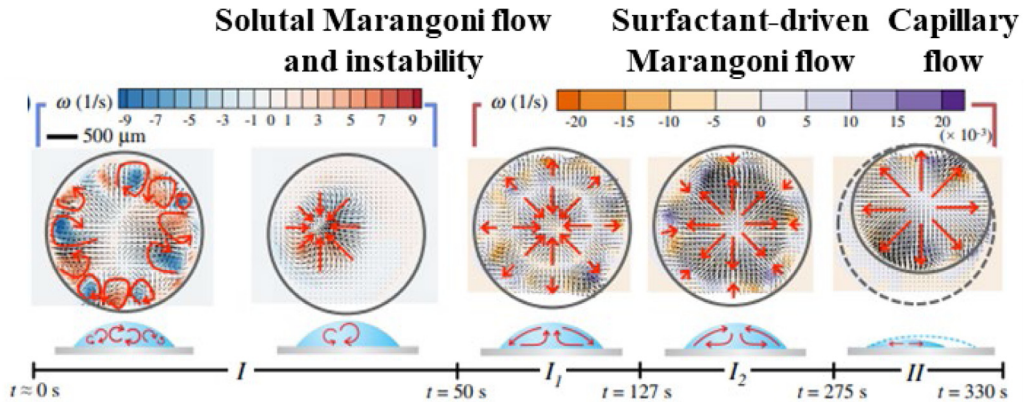
Fig. 11. Flow patterns at the bottom of a sessile ethanol–water (35:65 wt%, 0.60 ±0.07 μL) droplet with 0.05 wt% sodium dodecyl sulfate (SDS) [143].
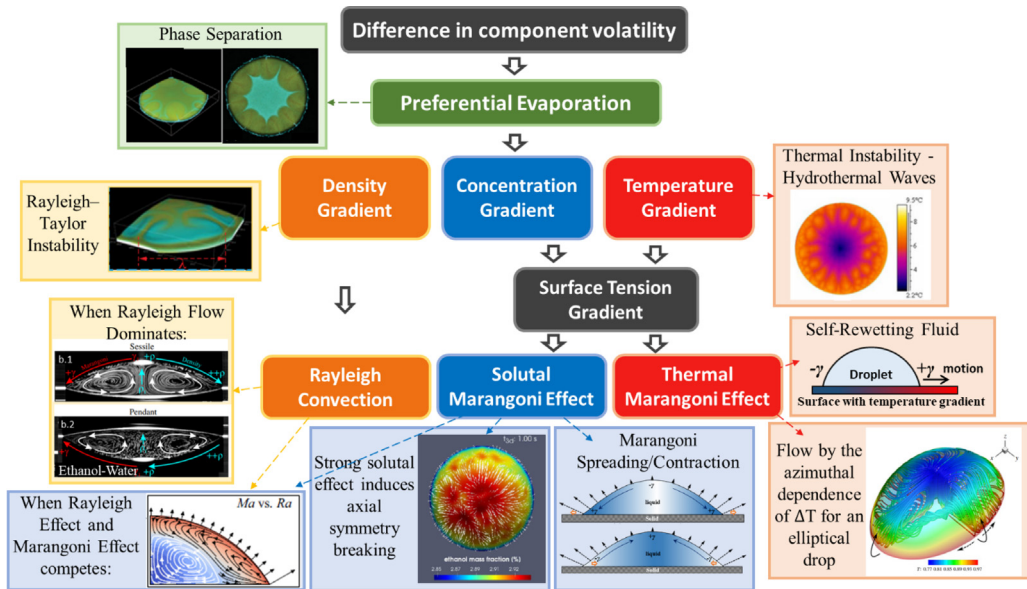
Fig. 12. A brief summary of key physical processes and the resulted phenomena taking place with evaporating multicomponent droplets [17,18,39, 47,136,140,141].

the size and geometry of the final depositions. Additionally, in a system consisting of 1,2-hexanediol, water and a minute amount of silicone oil [141], the non-volatile 1,2-hexanediol extracted into the oil accumulates at the rim of the droplet and hinders the evaporation therein. Consequently, the Marangoni flow is suppressed, and the gravitational flow plays a dominant role, which explains the Rayleigh–Taylor instability (plumes of 1,2-hexanediol) arising from the rim of the sessile droplet during evaporation.

2.3.4. Droplets with nonvolatile components

When it comes to aqueous solution droplets, the relative strength of solutal Marangoni convection and Rayleigh convection relates to the droplet shape and the component properties [146–149]. For typical saline solutions such as sodium chloride–water mixture (NaCl-H_2O), the surface tension and mass density increase with the salt concentration. Compared to the variation of surface tension in the case of a binary volatile droplet, the variation of surface tension during the evaporation of a saline solution droplet is much smaller. For example, the surface tension of NaCl-H_2O solution increases from 72.8 mN/m to 79.9 mN/m (*c.a.* 7.1 mN/m change), and the density increases from 998 kg/m^3 to 1148 kg/m^3 (*c.a.* 150 kg/m^3 change) as the mass fraction of NaCl increases from 0% to 20% (the critical saturation mass fraction is *c.a.* 26.4%) at 20 °C. By comparison, the surface tension of an ethanol–water solution increases drastically from 22.3 mN/m to 72.8 mN/m (*c.a.* 50.4 mN/m change), and the density increases from 789 kg/m^3 to 998 kg/m^3 (*c.a.* 209 kg/m^3 change) as the mass fraction of ethanol decreases from 100% to 0% at 20 °C. These data indicate that the solutal Marangoni effect (by surface tension gradient) in an evaporating saline solution droplet is typically weaker than that of an evaporating binary volatile droplet. Due to this reason, the gravitational effect is commonly acknowledged as much stronger than the solutal Marangoni effect in an evaporating saline solution droplet as concluded earlier by several individual groups [146,147]. By contrast, the gravitational effect in an evaporating binary volatile droplet is only proved to be significant in very recent studies [47,48], since it is somehow cloaked by the strong Marangoni effect and hence easily neglected in previous research.

Additionally, when the concentration of dissolved salt is high, crystallization takes place along with droplet evaporation. μ-PIV experiments by Efstratiou et al. [150] demonstrate the appearance of a remarkable jet of fluid directed at the point of nucleation. The jet is attributed to the competition between solutal Marangoni convection and the mass-conservation flow, which subsequently leads to the formation of vortices in the vicinity of the crystal. The phenomenon is observed to be universal for sessile droplets with initial contact angle up to 40°. Solutal Marangoni flow along with interfacial aggregation is also found to be the dominating mechanism of ring-shaped stains from evaporating chaotropic salt solution droplets, instead of the classical, capillary flow based "coffee-ring effect" [151].

To summarize, the addition of extra components increases the complexity of both wetting dynamics and evaporation behaviors of all kinds of multicomponent droplets. The influencing factors, dominating mechanisms and resulted phenomena are summarized in Fig. 12. With proper utilization of the interacting mechanisms, it is possible to tune the droplet behaviors for many practical applications. Besides the evaporation-induced phenomena, the droplet dynamics and evaporation performance can also be influenced by adjacent droplets or external vapor sources. In the next section, we will introduce the interesting mechanisms involved with those topics, namely vapor-mediated droplet wetting and vapor-mediated evaporation behaviors.

3. Vapor mediated droplet wetting and evaporation behaviors

Evaporation takes place driven by the vapor pressure gradient from the droplet surface to the unsaturated atmosphere. By tuning the concentration field at the gas phase, *e.g.* with external vapor sources, it is possible to control the direction and magnitude of the interfacial mass flux, thus manipulating the droplet wetting and evaporation dynamics. For adjacent volatile droplets, "communications" via the ambient and via the solid substrate can be realized through the interaction of vapor and temperature fields [152–156]. In the past decade there has been a vast increase in the number of publications on the ambient or substrate mediated interactions and/or vapor mediated interactions. In this section, we provide an extensive view on the vapor-ambient and/or vapor-substrate mediated interactions. The potentials and colorful mechanisms ensuing with these interactions are summarized and highlighted.

3.1. Interaction between adjacent droplets

3.1.1. Droplet lifetime

Most of the work to date on the evaporation of multiple droplets has been carried out for single component droplets. As early as in the 1990s, researchers [152,153] found that the volatile droplets in ordered arrays experience a phenomenon of "cooperative evaporation", which evidences the strong connection between adjacent droplets through the vapor field. For droplet arrays of the same component, the boundary conditions at the vapor phase differ greatly from the vapor-phase boundary condition of a single droplet. Due to the evaporation of adjacent droplets, the vapor field is an overlap of the initial atmospheric condition and the diffused vapor flux from the droplet arrays. As a result, the mass flux at the droplet interface is suppressed at the area near its droplet neighbors [154,155] (Fig. 13a).

Due to the suppression of interfacial mass flux, droplets in a droplet array with close distance between each other usually indicate longer lifetime than that of a single droplet [159]. Moreover, due to the shielding effect of adjacent droplets, the evolution of the droplet profile and the depositions of droplet arrays follow a universal routine, shown as the droplet with the most overlaps of vapor field evaporates the most slowly and vanishes at the last moment as shown by Fig. 13b where the droplet sitting in the middle of the array evaporates last [157,158]. Theoretical and mathematical modeling on this topic (evaporation of droplet arrays) has been carried out by Schäfle et al. [153] and Wray et al. [158] which indicate a good prediction accuracy.

For droplets evaporating in static air, the natural convection by the buoyancy effect is usually weak, which can be characterized with low Rayleigh number, Ra~0.1. In such cases, diffusion dominates the mass transport in the gas phase,
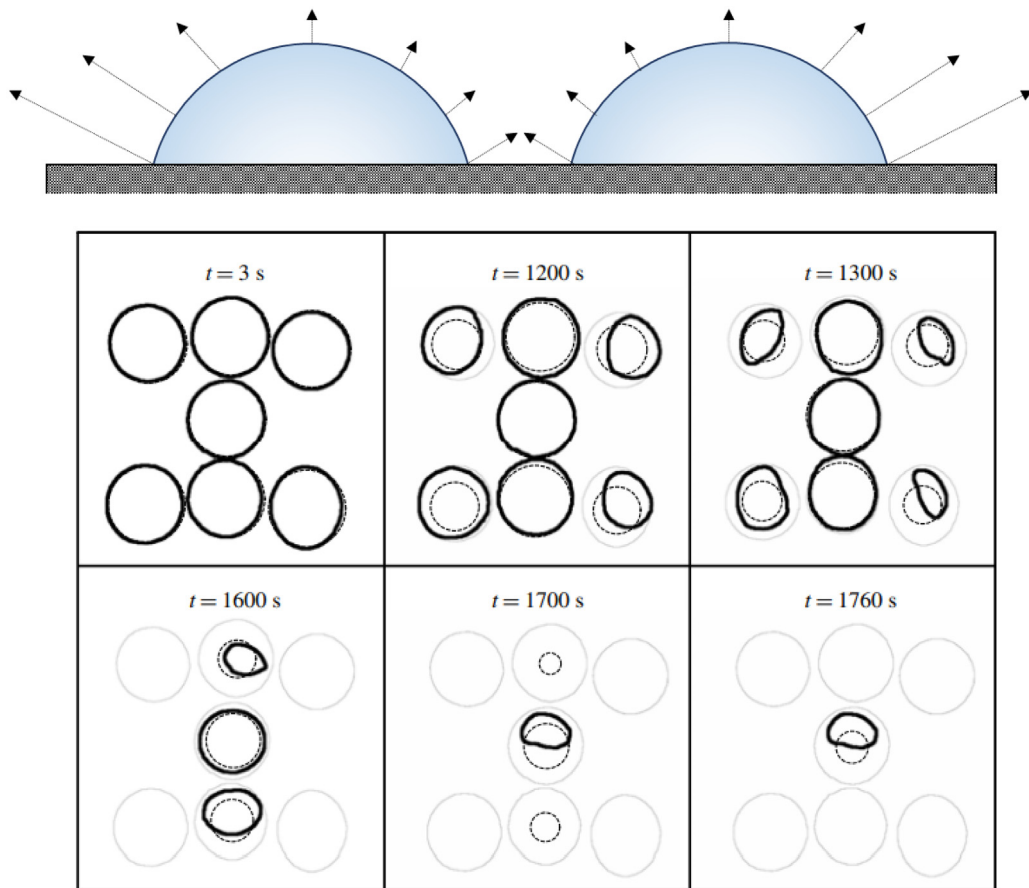
Fig. 13. (a) Distribution of mass flux in the case of two neighboring sessile volatile droplets; (b) Planform of seven droplets in an 'I'-shaped configuration at six different dimensional times (in seconds): Comparison between the experimental results by Khilifi et al. [157] (solid lines) and the theoretical predictions by Wray et al. [158] (dashed lines).

and the vapor accumulates among the droplets, causing the shielding effect as introduced before. However, when the density of the solute fluid is considerably less than that of the host fluid, *e.g.* the dissolution of multiple alcohol droplets in water (Ra~100), the collective convection will form a merged concentration plume and strengthen the dissolution process, similar to the strong merging flames from nearby candles [160].

3.1.2. Droplet dynamics

The influence of adjacent droplets via the vapor field can also be strong enough to drive droplet motion on high-energy surfaces without contact line pinning. Experiments on binary droplet interactions [78] by Cira et al. and later by other research groups [161,162] indicate that the nonuniform evaporation mass flux due to the different vapor-mediated interaction induces concentration gradients across both droplets. Depending on the composition of the interacting droplets, the droplets will attract or repulse each other at long range and coalesce or chase each other at short range. Fig. 14 depicts the representative dynamics of two adjacent propylene glycol (PG)-water droplets with different PG-water compositions. Compared to PG, water has apparently higher vapor pressure and contributes to the humidity gradient in the gas phase. At long distance (Fig. 14a), the two droplets correspond to the humidity gradient, and the water concentration at the inner side near each other is high due to the suppressed evaporation mass flux (water vapor) there. Since the surface tension of water is much larger than that of PG, the local surface tension increases, which drives the droplets to move towards each other. As the two droplets get close enough, a small amount of mass exchange happens through the precursor film or by direct contact. For droplets of similar concentrations, the droplets coalesce after the initial contact. For droplets with apparently different concentrations, the small amount of mass exchange induces concentration gradients across both droplets and drives the low-surface-tension droplet to chase the high-surface-tension droplet as indicated by the "short-range interaction" in Fig. 14b.

In addition to the interacting movement of binary liquid droplets, researchers [156,162] have demonstrated that the vapor-mediated motion can also take place in the case of adjacent pure liquid droplets without the solutal Marangoni
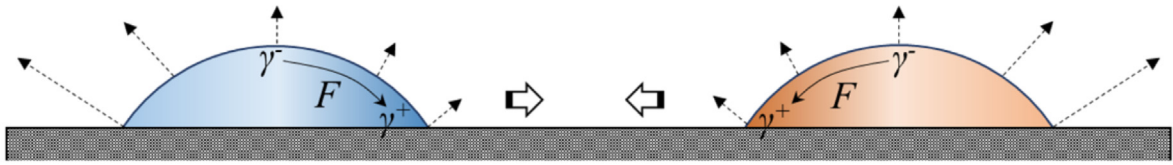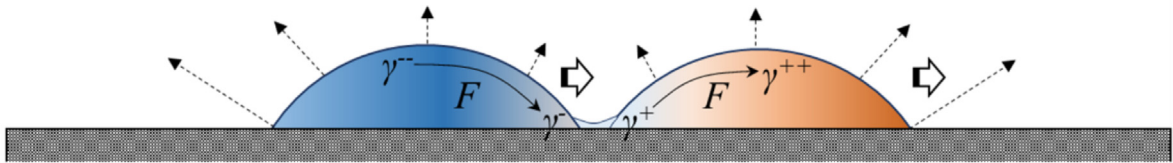
Fig. 14. (a) Long-range and (b) short-range interactions between two adjacent propylene glycol (PG)-water droplets with different PG concentrations on a smooth high-energy surface [78,161]. The orange droplet (right side droplet) has low PG concentration and hence high surface tension, while the blue droplet has high PG concentration and low surface tension. The dotted arrowed lines indicate the interfacial water mass flux. The solid arrowed lines indicate the direction of the driving force from low to high surface tension regions. The striped hollow arrows indicate the direction of droplet motion.
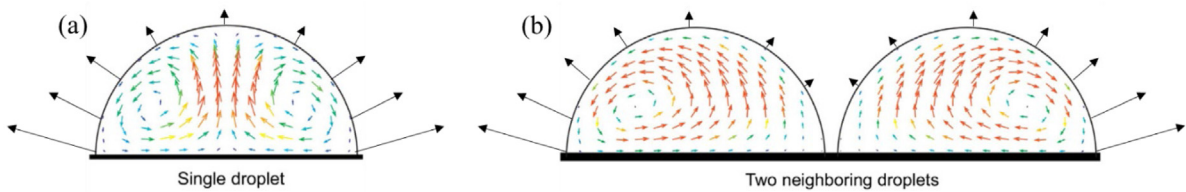

Fig. 15. Flow patterns inside droplets of aqueous NaCl solution undergoing evaporation: (a) a single droplet and (b) two neighboring droplets. [163] For a single NaCl Droplet, a surface tension gradient forms from the low NaCl concentration at the apex towards the high NaCl concentration at the contact line due to the large evaporation mass flux there. In the case of two neighbor droplets, evaporation is suppressed on the side near its neighbor with greater NaCl concentration at the opposite edges of the droplet pair, which induces the symmetry breakage of the internal flow.

effect. Theoretical predictions are proposed by Man et al. [164] based on the gradient of evaporation mass flux across the droplet. Specifically, the non-uniform evaporation rate drives droplet motion from the high-evaporation-flux side to the low-evaporation-flux side, so as to reduce the energy dissipation associated with the inherent fluid flow induced by evaporation. Additionally, Sadafi et al. [156], in their study, reported observations and phenomena owed to substrate-mediated forces, including the thermocapillary effect by non-uniform substrate temperature and the variations of evaporation-induced contact angles. Those studies evaluate the potentials of various influencing factors on the droplet motion and provide solid theoretical supports for the non-contact control of droplet dynamics in lab-on-a-chip processes.

3.1.3. Flow patterns

For single droplets undergoing evaporation in ideal conditions (ideally uniform ambient environment, droplet shape and substrate condition), the internal flow patterns are symmetric as represented in Fig. 15a. With the presence of an adjacent volatile droplet, the symmetry is disrupted, and the vapor field changes significantly. As shown in Fig. 15b, for adjacent NaCl-H_2O droplets, the salt concentration at the side far from its neighbor is high due to the large evaporation mass flux there. The arising surface tension gradient at the droplet surface drives an interfacial flow towards the side with large mass flux [163].

As a result of the convective particle transport, it is evidenced [165] that the depositions at the closest region of two colloidal droplets are apparently weaker compared to the rest of the region (Fig. 16). Similar effect can also be found in adjacent condensing droplets as recently reported by Pradhan and Panigrahi [166].
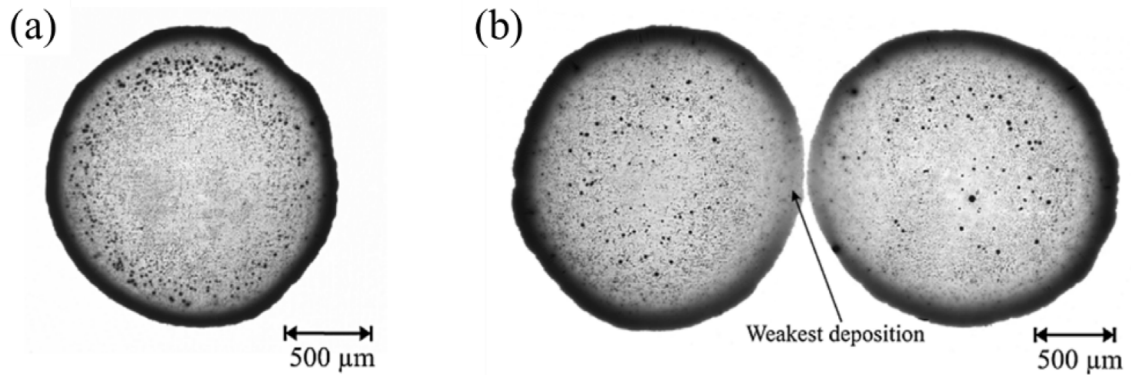
Fig. 16. Deposition patterns of dried droplets with ink dyes: (a) a single droplet and (b) two neighboring droplets with a separation distance of 25 µm [165]. Single droplet configuration shows uniform deposit along the contact line after drying. In the presence of a neighboring droplet, the deposition pattern is not uniform along the contact line, shown as, the deposition at the nearest point of the two droplets is weakest as compared to the rest of the contact line.
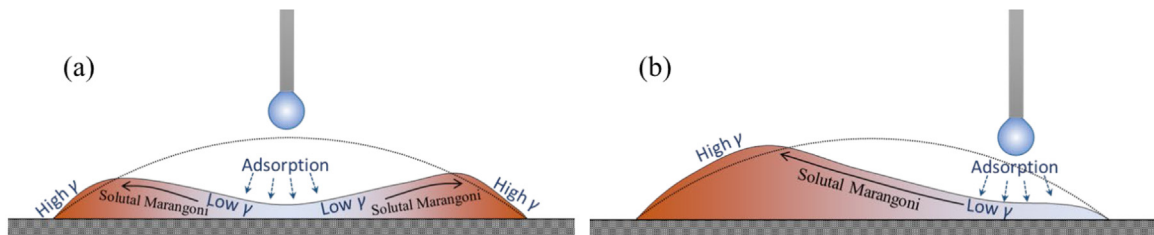

Fig. 17. Behaviors of a thin water droplet on a highly wettable substrate in response to a pendant ethanol droplet (a) near the center, and (b) near the edge of the sessile droplet. [167] The pendant ethanol droplet behaves as an external vapor source. As the ethanol vapor adsorbs onto the surface of the sessile droplet, the surface tension at the nearby area decreases, which drives a solutal Marangoni flow towards the high surface tension region and causes the deformation and deviation of the sessile droplet, which can eventually cause droplet splitting or droplet motion.

3.2. Manipulation through external vapor sources

3.2.1. Droplet dynamics

Besides the influence of adjacent droplets, the droplet behaviors can be actively tuned with external vapor sources. As shown in Fig. 17 [167], a thin water droplet on a highly wettable surface is driven to move in response to an adjacent pendant ethanol droplet. In this system, the volatile pendant ethanol droplet behaves as a source of ethanol vapor. The diffusing ethanol vapor gets adsorbed into the water droplet and reduces the surface tension at the nearby region. When the ethanol source locates near the edge of the water droplet (Fig. 17b), the Marangoni effect will shift the liquid to the other side of the droplet with higher surface tension. In specific cases, *e.g.* when the ethanol source is placed near the center of the droplet (Fig. 17a), the induced solutal Marangoni flow can be strong enough to deplete the liquid at the droplet center and lead to droplet splitting.

For liquid films on wettable solid surfaces, the external vapor source of low-surface-tension liquid, *e.g.* isopropyl alcohol (IPA), can lead the dewetting of the film due to arising concentration gradient at the film surface (Fig. 18) [168]. Besides the solutal Marangoni effect, researchers [169] have also pointed out that the high concentration of alcohol absorbed near the film center may expedite the evaporation of the thinning region and speed up the dewetting process.

Yet wetting dynamics with even higher complexity may be realized by proper manipulation of binary droplets (water-PG) via an external water vapor source [170]. By tuning the relative position between the water vapor source and the binary droplet, both attractive and repulsive droplet motion can be realized. With a simplified model based on the 2D functional form of the surface tension gradient, the authors attributed the controllable droplet motion to the arising solutal Marangoni flow as well as the symmetry breaking due to small displacement even when the vapor source is just above the droplet apex. A series of applications can be further developed taking advantage of this method for droplet manipulation and control. This may include directional printing as well as controllable chemical reaction of materials in a contactless way [170].

3.2.2. Flow patterns

Experiments with μ-PIV demonstrate the flow patterns inside a sessile droplet in response to external vapor sources, *e.g.* a sessile water droplet with an external ethanol vapor source. Due to molecule adsorption, for example, the adsorption
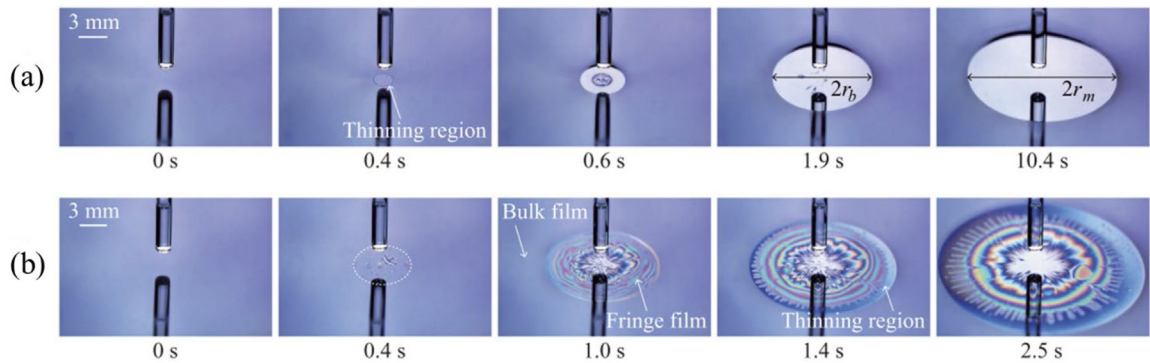
Fig. 18. Dewetting of water films induced by an external isopropyl alcohol (IPA) vapor source. (a) Initial film thickness of 260 µm and (b) Initial film thickness of 50 µm. The low liquid–air surface tension due to the adsorption of isopropyl alcohol (IPA) vapor in the region near the capillary leads to radially outward Marangoni flow. The receding bulk leaves a thin liquid layer in the center, which is punctured by evaporation. The thin layer is called a fringe film, and it is connected to the rim of bulk via a narrow region of further reduced thickness, called a thinning region. While thin films with $h_0 \sim 10$ µm exhibit the development of those distinct regions over 1 s, relatively thick films with $h_0 > 100$ µm show rapid drying of a thinning region, which first appears at 0.4 s. [168].
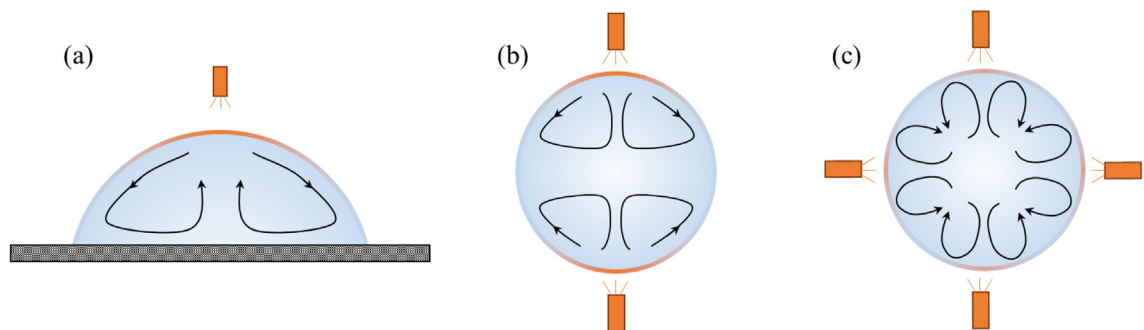

Fig. 19. Flow patterns induced by external vapor sources. (a) single vapor source above a sessile droplet (side view) [172], (b) two vapor sources on opposite sides of a sessile droplet (top view), and (c) four evenly distributed vapor sources (top view) [173]. When the needle is positioned close to the droplet's upper surface, ethanol vapor induces recirculating Marangoni flows (solid lines) due to a local reduction in surface tension. The number and occurrence of the vortices are then imposed and controlled by tuning the numbers and position of the vapor sources around the evaporating droplet. The solid arrow lines indicate the direction of the flows.

of ethanol vapor into a water droplet, the region near the vapor source exhibits low surface tension and the generated surface tension gradient induces vortices inside the droplet [171]. Fig. 19a indicates the flow vortices formed from low-surface-tension to high-surface-tension regions for one single vapor source sitting above an evaporating droplet. As the number of vapor sources increases, so does the number of vortices, demonstrating strong forced convection inside the droplet as in Fig. 19b and c. For droplets with colloidal suspensions, the deposition patterns from drying droplets can be tuned [172]. As indicated in Fig. 20, different deposition patterns form by properly designing the positions and pathways of external vapor sources. The enhanced convection by external vapor sources provide a low-cost and contactless approach for flow and deposition control in various chemical processes [173].

4. Experimental techniques

To reveal the dominating physical mechanisms along with droplet phase change, it is important to develop experimental techniques that can accurately track the evolution of key physical parameters both spatially and temporally. Table 2 lists the commonly applied experimental techniques in the study of droplet phase change. Typically, the basic information of droplet profile and its real-time evolution can be captured from the side by optical imaging while other techniques may additionally be coupled for a better understanding of the mechanisms taking place. The basic parameters of the droplet profile, i.e. contact radius, contact angle, and droplet height, can be extracted through image processing with self-developed programs or commercial software. The resolution of the image analysis depends on the resolution of the optical lens as well as on the camera resolution, i.e. pixel count, while the temporal resolution depends on the frame rate of the camera. The measurement error may arise from the image contrast, from the calibration error as well as from the accuracy of image processing. Countless are the research works to droplet evaporation where optical imaging has been applied, hence we do not provide the specific examples for this.
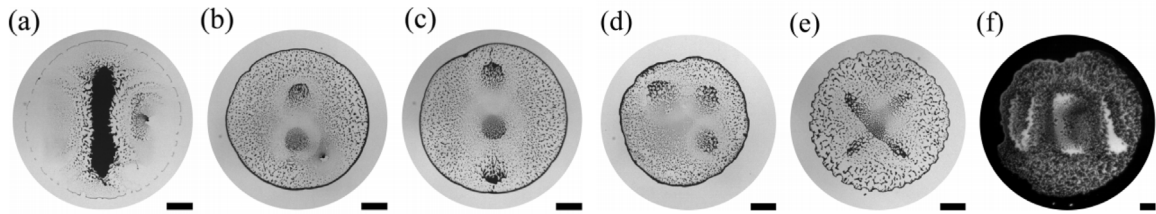
Fig. 20. Surface patterning formed form evaporating droplets by spatially shifting the ethanol vapor point source [172]. (a) a line, (b) two dots, (c) three dots in a line, (d) three dots in a 2D configuration, (e) a cross, and (f) the letters UCL. All patterning was performed using 1 μL droplets containing a 1 wt % water suspension of 2 μm monodisperse silica particles, except for (f) where a 3 μL droplet of a 1.5 wt % suspension was used. As vapor point source, a needle of 80 μm internal radius at h $\leq$ 0.75 mm was used, except in (a) where a needle of 210 μm internal radius at $h = 2$ mm was used instead. All scale bars correspond to 1 mm.

Table 2
Experimental techniques for the study of evaporating droplets.

Experimental Technique	Parameters	Working Principle	Spatial and Temporal Resolution
CCD (microscope) camera [Widely applied in droplet-related studies.]	Droplet height, contact radius, contact angle, etc.	Optical imaging	High spatial and temporal resolution can be realized with the combination of high-speed camera and microscopy
IR thermography [17,18,112, 113,120,127–129,174]	Interfacial temperature	Detecting infrared energy emitted from object, and converting it to temperature distribution	Temperature resolution better than 30mK, Frame rate up to $\sim$10^3 fps, Pixel size using coupled microscope up to 1.3 μm [175]
μ-PIV [39,47,48,78,134,137, 138,143,147,170]	Flow field	Extracting real-time velocity maps from the separate images of tracing particles illuminated by μ-PIV pulse laser	Spatial resolution $\sim$1 μm, frame rate up to $\sim$10^3 fps [176]
Optical coherence tomography (OCT) [47]	Flow field	Utilizing low-coherence light to capture micrometer-resolution 3D imaging of the droplet subsurface microflows	Spatial resolution $\sim$1 μm, frame rate up to $\sim$10^3 fps [47]
Background Oriented Schlieren (BOS) imaging [177,178]	Density	Mapping the density field by capturing the deformation of background pattern (pixel shift) due to light refraction.	Depending on the background pattern and the pixel of the digital imaging [177,178]
Fourier transform infrared spectrometer (FTIR) [179]	Gas-phase concentration field	Mapping the concentration field at the gas phase based on the relation between the absorbance and vapor concentration	Depending on the accuracy of the calibration curve between absorption rate and vapor concentration [179]
Gas injection chromatography [112,180]	Average concentration	Based on a partition equilibrium of analyte between a viscous liquid stationary phase and a mobile gas	$\leq$5% [112,180]
Refractometer [181–185]	Concentration field/ Temperature field	Measuring the concentration of liquid mixtures based on the refractive index calibration curve constructed beforehand	Resolution of refractometer is $\sim$0.1%, while it also depends on the accuracy of calibration of the refractive index-concentration curve [181–183]
Visualization by dissolving particles [40]	Concentration field	Tracking the concentration field during polystyrene particles dissolution on Pyrrolidinone-deionized water mixture.	Depending on the resolution of CCD camera (microscopy)
Confocal microscopy [39,44,45,48,186]	Distribution of different components	Labeling individual components with fluorescence dyes and mapping the distribution of different components with illuminating laser in a 3D view.	Pixel depending on the imaging camera; Frame rate up to 10^2 fps at fast modes.

The accurate mapping of interfacial temperature is crucial in studies on the thermal effect induced by liquid-vapor phase change. Conventional thermocouples can be utilized for direct temperature measurement within the droplet, in which case the thermocouple bead diameter should be as small as possible in order to minimize its disturbance to the droplet profile and to improve the time sensitivity. Non-contact temperature mapping can be realized by IR thermography. Compared to conventional thermocouples, the IR thermography is able to map the temperature distribution across the droplet surface instead of specific points. However, the accuracy of IR thermography is affected by the surface condition

of the object as well as the environmental temperature and relative humidity. Corrections are needed when doing the measurements in order to eliminate the deviations brought by the environment and the property difference between different materials. In practical applications, a combination of thermocouples and IR thermography can be utilized to trace the evolution of both interior and interfacial temperatures according to the actual requirement of the experiments. The use of IR thermography revealed the occurrence of hydrothermal waves induced by interfacial phase change [17,18] and its fade when a pure ethanol evaporating droplet transitions into a water droplet as a consequence of the absorbed/adsorbed and/or condensed water [112,113].

The μ-PIV technique is a representative and powerful approach to trace the flow field inside an evaporating droplet. This technique evaluates the velocity field within a droplet by tracing the motion trajectories of fluorescence particles distributing in the fluid. In a conventional double-pulse-type μ-PIV system, the measurement depth (MD) is considerably thick, which means that the light intensity of particle images is strong enough to affect the velocity measurement. Therefore, the multiple velocity components included in the thickness of the MD cause errors. With the assistance of confocal laser sheet (confocal scanning μ-PIV), it is possible to narrow the thickness of the MD to include only one velocity component, thus making the measurement clear and accurate. The utilization of μ-PIV has made it possible to reveal the detailed flow pattern transitions during the evaporation of binary volatile droplets, *e.g.* an ethanol–water droplet [137], during the crystallization of saline solution droplets [187], as well as in the evaporation of Ouzo droplets [44,45,144] and other complex droplets [143]. For more details on the flow patterns inside multicomponent droplets, the readers are referred to Section 2.3 in this review paper.

The mass diffusion and convection induced by concentration gradients usually outweigh the thermal effect in an evaporating multi-component droplet, therefore it is of great significance to explore new experimental techniques for accurately mapping the concentration field inside and outside the droplet so to provide some further insights on the magnitude and strength of the Ma_s and Ma_{th}. T. The gas chromatography is a typical technique utilized initially in analytical chemistry for separating and analyzing compounds that can be vaporized without decomposition. With the assistance of this technique, it is possible to trace the average concentration of a binary volatile droplet [112,180], while it is difficult to map the concentration distribution. To date, the gas chromatography has made it possible to trace the concentration evolution of individual components inside a droplet, so that we can correctly predict the lifetime of a multicomponent droplet with the developed semi-empirical correlations [112]. More details on the semi-empirical correlations proposed for multicomponent droplets are referred to Section 5 of this review.

Yet another technique for tracking the average liquid concentration within a droplet is the refractometry. The refractive index is a dimensionless number that describes how fast light travels through a medium, and the refractive index of a liquid mixture is directly correlated to the component composition. By mapping the measured refractive index with the refractive index-concentration curve established beforehand, the refractometer can reveal the in-time solute concentration of the liquid mixture. The resolution of refractometer depends on the accuracy of the calibration curve where considerable derivations may exist, while its merit lies in the outstanding time sensitivity. The refractometer has been utilized especially in the component tracing of fuel droplets in combustion applications [181,183]. With the gas chromatography and refractometer, it is possible to trace the variation of the average concentration of an evaporating droplet, and the accuracy is based on the assumption that the droplet is fully mixed, which is not the real situation in most practical cases as it was conveyed in earlier sections.

To map the concentration distribution within a droplet, researchers have been actively seeking for alternative techniques based on various working principles. Kim and Stone [40] take advantage of the special property of fluorescent polystyrene particles which dissolve in 1-Methyl 2-Pyrrolidinone (1M2P) and deionized water mixture above a critical concentration of 90 wt% 1M2P. For a sessile 1M2P-water droplet decorated with polystyrene particles, the concentration of 1M2P near the TPCL increases due to the preferential water evaporation therein. As the concentration of 1M2P exceeds the critical concentration, fluorescent polystyrene particles dissolve. By tracing the distribution of polystyrene particles, it is possible to visualize the preferential distribution of interfacial mass flux and the evolution of interfacial concentration. However, such method is merely applicable to one specific type of multicomponent droplets while the concentration field of other types of multicomponent mixtures cannot be traced.

Confocal laser scanning microscopy, widely applied in biomedical studies, provides a more general approach for tracing the concentration field. This technique firstly labels the different components in a liquid mixture with fluorescent dyes, then visualizes the distribution of the individual components through laser illumination with corresponding excitation wavelengths. The observation can be conducted in the form of both two-dimensional (2D) and three-dimensional (3D) images. The 2D images are obtained by focusing the microscope horizontally near the liquid–solid interface, while the 3D images can be obtained by reconstructing a series of consecutive Z-stack 2D images scanned from the bottom to the top of the droplet. The time sensitivity of high-speed confocal microcopy is appropriate for this type of investigations. In the study of Li et al. [39,141], the scan rate of 2D mapping is 30fps, while a loop of 3D mapping in the z-stack takes about 4 s, which is sufficient for the observation of concentration field during the evaporation of a multicomponent droplet. With the assistance of the confocal laser scanning microscopy, researchers have been able to observe the phase segregation phenomena induced by fast water evaporation in a binary volatile droplet [38,39,141], as well as the phenomena of oil nucleation in an evaporating Ouzo droplet [44,45,144]. Powerful as it is, the confocal microscopy is only applicable for droplets composed of liquids that can be dyed by fluorescence, such as lipid liquids that can be dyed with Nile red and polar solvents in which specific fluorescent dyes (*e.g.* Dextran) can dissolve. Additionally, the accurate quantitative evaluation of the concentration distribution remains a challenge.

It can be seen that efficient experimental techniques are still lacking for mapping the concentration field of a wide range of multicomponent droplets. From the fundamental point of view, the similarity of different liquid molecules makes it difficult to distinguish by their normal optical properties or mechanical properties. Approaches such as confocal microscopy detect the feedback signals of different liquid molecules in response to external excitations, while accurate quantitative characterization is still of great difficulty. To counteract some of the deficiencies and the impossibility to resolve certain mechanisms via existing experimental techniques, mathematical models have been of extreme importance which are reviewed in the subsequent section, Section 5.

5. Review of existing models

Numerical models on the wetting, phase change, and contact line dynamics of single component droplets have been well developed in the past decades. Since a thorough review on all the relevant models to droplet behaviors would be lengthy and deviates from the focus of this paper, here we mainly focus on available models of multicomponent droplets with interfacial phase change. Additionally, a general overview on the numerical methods and the key issues is given instead of exhaustive briefing of each relevant work. For the numerical models of single component droplets, the reader is referred to the review paper by Erbil [58].

For multicomponent droplets, the concentration variation of individual components plays a crucial role. The concentration gradients induced by the preferential evaporation cause severe variation of liquid density, viscosity and surface tension, thus dominating the flow states of the droplet. The phase change and fluid flow subsequently affect the interfacial temperature and liquid composition, causing the spatial–temporal variation of evaporation mass fluxes. These factors combined make the problem more complex than the single-component cases, and it is impossible to derive an analytical solution. Up to now, models for the evaporation of multicomponent droplets involve numerical models established with commercial software (available for limited types of liquid mixtures) or direct numerical simulation (DNS), as well as simple empirical or semi-empirical models based on the experimental data.

5.1. Numerical models

5.1.1. Governing equations
The numerical modeling of a sessile evaporating droplet can be divided into three domains: the liquid domain (droplet), the gas domain (ambient) and the solid domain (substrate) as shown in Fig. 21. For a multicomponent droplet, the physical processes in the liquid domain demonstrate the highest complexity, where the spatial distribution of different species leads to complex convective flows along with the thermal effect and the gravitational effect presented by natural convection. Taking all the necessary effects into account, the governing equations of the liquid phase include the Navier–Stokes equations (conservation of mass and conservation of momentum) which describe the internal flows (Eqs. (3) (4)),

$$\frac{\partial \rho}{\partial t} + \nabla \cdot (\rho \boldsymbol{u}) = 0, \tag{3}$$

$$\rho \left(\frac{\partial \boldsymbol{u}}{\partial t} + \boldsymbol{u} \cdot \nabla \boldsymbol{u} \right) = -\nabla p + \nabla \cdot \left(\mu \left(\nabla \boldsymbol{u} + \nabla \boldsymbol{u}^T \right) \right) + \rho \boldsymbol{g}, \tag{4}$$

the energy equation which describes the thermal transport process (Eq. (5)),

$$\rho c_p \left(\frac{\partial T}{\partial t} + \boldsymbol{u} \cdot \nabla T \right) = \nabla \cdot (k \nabla T), \tag{5}$$

as well as the concentration equation which indicates the advection and diffusion transport of different components (Eq. (6)),

$$\frac{\partial x_A}{\partial t} + \boldsymbol{u} \cdot \nabla x_A = \nabla \cdot (D_A \nabla x_A), \tag{6}$$

where $\boldsymbol{u} = (u)$, is the velocity vector in a cylindrical coordinate system, and u, v, and ω correspond to the horizontal, azimuthal and vertical components of the velocity field, p is the liquid pressure, μ is the liquid viscosity, g denotes the gravitational acceleration, c_p denotes the heat capacity of the liquid, k is the thermal conductivity, x_A is the concentration of component A, and D_A is diffusion coefficient of component A in the liquid mixture. For a droplet with n components, the compositional concentration should also meet the conservation law, namely, $\sum_{i=1}^{n} x_i = 1$, therefore, $(n-1)$ equations for solute concentration are actually needed to fully describe the mass transport in the liquid phase.

In atmospheric environments, the gas phase can be regarded as a mixture of dry air and water vapor. Depending on the dominating mechanisms of the target system, the mathematical description of the gas phase can be reasonably simplified. For a sessile droplet evaporating in steady air with a temperature far below the boiling point, the air convection is usually very weak as well as the Stefan flow. Therefore the mass transport can be simplified into pure vapor diffusion expressed by the Fick's law of diffusion, Eq. (7). The assumption has been widely applied in a number of numerical models [19,188,189]
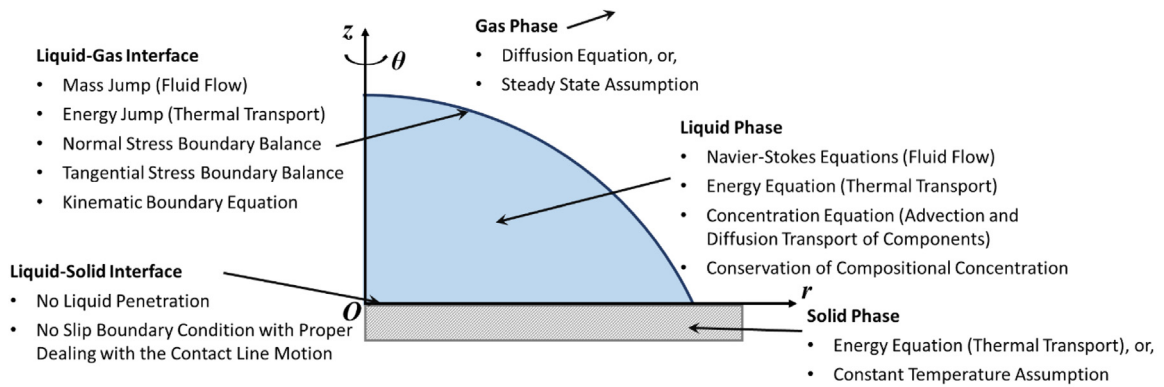
Fig. 21. Governing physical processes in an evaporating multicomponent droplet taking all three phases (liquid, gas, and solid) into account.

describing droplet evaporation and has proved to be valid both in the prediction of the evaporation rate and in capturing the dominating processes.

$$\frac{\partial y_A}{\partial t} = D_{A,\text{vapor}} \nabla^2 y_A, \tag{7}$$

where y_A denotes the vapor concentration of component A and $D_{A,\text{vapor}}$ presents the diffusion coefficient of component A in the gas phase.

Compared to the liquid phase, the density, viscosity, and thermal conductivity of the gas phase are significantly smaller, namely, $\rho_v \ll \rho_l$, $\mu_v \ll \mu_l$, $k_v \ll k_l$. Moreover, the mass diffusion rate in the gas phase is $10^3 \sim 10^4$ times of the rate of solute diffusion in the liquid phase [190]. Consequently, in some numerical models, the state of the gas phase is regarded as homogeneous, and the model focuses on the governing physical mechanisms in the liquid phase, namely the one-sided model as described later in Section 5.1.5.

The mathematical description of the solid substrate is relatively simple where mainly the thermal transport process should be considered. When a temperature-controlled module is applied or when the thermal conductivity of the material is very high, the solid substrate can be dealt as a constant-temperature object. For a substrate consisted of ordinary materials, the temperature field inside the substrate can be solved based on the energy equation with all the surrounding boundary conditions well defined.

Besides the physics within the three phases, correct descriptions of the interfacial phenomena are of equal importance. Especially, at the liquid–gas interface, phase change takes place, which induces mass jump of different species (①) as well as energy jump due to the latent heat release (②). Additionally, the preferential evaporation of individual components in the case of multicomponent droplets also induces concentration and temperature gradients at the liquid–gas interface and results in surface tension gradients. Therefore the normal stress boundary balance (③) and tangential stress boundary balance (④) need to be properly defined taking account of the arising interfacial flow and the shear stresses. The interfacial phase change can also induce the movement of the liquid–gas interface. To relate the fluid flow with the interface motion, a kinematic boundary equation (⑤) should be derived which demonstrates the relationship between the flow velocity vector with the interfacial mass flux. For different type of liquid mixtures, equations accounting for the different physical phenomena introduced from ① to ⑤ should be formulated accordingly. Readers are referred to the work of Diddens et al. [136,140,188,189] and Williams et al. [110,191] for the mathematical formulation of a binary volatile droplet system as well as the work of Wang et al. [192] for the formulation of an aqueous saline solution droplet system.

At the liquid–solid interface, a no-liquid-penetration boundary equation should be applied. Additionally, as droplet phase change takes place, a relative motion between the liquid and the solid substrate especially near the TPCL is expected, which counteracts with the no-slip boundary equation that is typically applied at the liquid–solid interface. To solve this problem, we need to properly deal with the motion of the contact line, so that the singularity in numerical calculations can be avoided and the dynamic of the droplet can be correctly predicted. In the past decades, several approaches have been proposed by individual groups, with corresponding advantages and disadvantages. A brief review of the available approaches for moving contact line are given later in Section 5.1.4.

It should also be noticed that necessary simplifications are always needed to solve the interacting physical processes while maintaining the characteristics of the dominating mechanisms. At the liquid–gas interface, the transition of vapor molecules from liquid to vapor generates an inward normal force, namely the vapor recoil effect, which is evidenced to be a destabilizing factor of interface dynamics [193]. Nevertheless, the recoil force is practically only important for applications with very high mass fluxes [194]. For droplet evaporation, the vapor pressure difference across the liquid–gas interface is in the order of several kPa. Therefore the inward pressure exerted by vapor recoil is relatively weak and resisted by capillary and Marangoni effects, thus can be reasonably omitted in model formulation [192].

Yet some other simplifications are also frequently applied according to the practical needs of different numerical models. For example, in the simulation of binary volatile droplets by Diddens et al. [189,190], the mass density of the liquid mixture is approximated by the spatially averaged composition as the model mainly focuses on the phenomena of interfacial phase change and the internal flow patterns. This allows the simplification of the convection–diffusion equation and the momentum equation. In the simulation of binary droplets by Williams et al. [110] and saline solution droplets by Wang et al. [192], the Kármán–Pohlhausen integral approximation is applied, where the fluid velocity and temperature are approximated by a polynomial of the form $c_1 + c_2 z + c_3 z^2$ and the variables are integrated in the z direction. By doing this, the multiple variable differentials are removed while the inertia and advection terms in the momentum and energy equations remain. Additionally, the concentration distribution can also be approximated in the corresponding polynomial form (rapid diffusion or weak diffusion) based on the evaluation of the diffusion strength, *i.e.* the value of Peclet number. Such rational simplifications help to reduce the complexity of the mathematical model, making it possible to correctly capture the dominating mechanisms while with a modest demand of computational resources.

5.1.2. Composition-dependent properties

The thermophysical properties of multicomponent liquid depend on the properties of individual components and their proportions/compositions. Proper correlations are needed to relate the important thermophysical properties, including viscosity, thermal conductivity, heat capacity, density and surface tension, with the concentration of different species as well as the local liquid temperature. Specifically, the relations for the concentration and temperature dependent liquid properties can be derived from the existing experimental data. For the property data of water–ethanol mixtures, the readers are referred to Refs. [195–199]. For water–glycerol mixtures, the readers are referred to Refs. [198–202]. For aqueous saline solution, experimental data of liquid properties can be found in Ref. [203] for NaCl-H_2O solution and in Refs. [204,205] for hygroscopic LiBr-H_2O solution, etc.

It is important to stress that, even though most of the thermophysical properties are function of both the liquid composition and the temperature, the influence of liquid composition is usually larger than that of the liquid temperature. In some of the numerical models, the liquid properties are approximated merely by its relation with the component concentration while the effect of liquid temperature is reasonably omitted for simplification purposes [189].

5.1.3. Tracking the liquid–air interface

For an evaporating multicomponent droplet, the phenomena at the liquid–air interface are most attractive, where the preferential evaporation of individual components induce a force imbalance and consequently complex interfacial flows. The interfacial forces can also be strong enough to deform the interface, affect the droplet dynamics and sometimes cause spontaneous droplet motion or droplet splitting. To track the dynamics of the liquid–air interface, necessary methodologies are needed. One of the most widely applied options is the lubrication theory, which is a convenient method to deal with the governing equations and boundary conditions with coupled variables. The lubrication theory assumes the geometric length of one specific dimension as apparently smaller than the others, so that the inertia terms in the Navier–Stokes equations can be neglected. Based on the lubrication theory, researchers established models for pure liquid droplets [13,206], binary volatile droplets [110,188,191], droplets with soluble and insoluble surfactants [99,207,208], as well as droplets with insoluble colloids or soluble salts [192,207,209–211]. The lubrication-type models can capture the main physical processes and well predict the droplet dynamics and interfacial parameters. However, the main overlaying assumptions make the lubrication-type models applicable merely for droplets with small or at least moderate contact angles (typically less than 40°).

For droplets with large contact angles, *i.e.*, on hydrophobic substrates, some other assumptions are needed to trace the evolution of the droplet profile and to solve the governing equations. One typical approach is to assume the sessile droplet as a spherical cap [17,189,190], which is reasonable for droplets sitting on a smooth flat homogeneous surface with contact radius below the capillary length. By applying the spherical cap assumption, the droplet profile can be assumed as a 3D sphere and the real-time droplet volume, droplet radius and contact angle are thus closely related. In terms of droplets evaporating in CCR mode, the contact angle can be derived according to the real-time droplet volume and the constant contact radius. While for droplets evaporating in CCA mode, the real-time contact radius can be predicted according to the droplet volume and the constant contact angle. Additionally, for models adopting the spherical cap assumption, empirical relations are needed between the dynamic contact angle and the velocity of the moving TPCL. Besides, the real-time droplet volume can be determined at each time step combining the derived interfacial mass flux and the droplet volume at the previous moment.

By comparison, the lubrication-type models are more suitable for tracing the distribution of interfacial parameters so that it can well explain some complex droplet dynamics especially at small contact angles. The spherical cap assumption, on the other hand, can be applied for a wide range of contact angles and behaves better when dealing with the Marangoni and natural convections inside the droplet. Nevertheless, it is not suitable for predicting complex droplet dynamics with highly deformed interfaces, such as sliding droplets on substrates with inclinations or with temperature gradients, as well as droplets with complex wetting dynamics or spontaneous motions.

5.1.4. Solutions for moving contact line

For tracing the dynamics of TPCL, an inherent contradiction exists in simultaneously assuming the no-slip boundary condition and the expected displacement between the liquid and solid interface. Therefore a force singularity will arise at the vicinity of TPCL as revealed in the study of Dussan and Davis [212]. To solve this problem, one typical approach is to establish a relationship between the advancing contact angle and its velocity based on the empirical correlations derived by experiments. In this case, reliable functions between the dynamic contact angle and the contact line motion are required to give a complete physical description of the problem. Representative work with this approach is referred to [213–215].

A different, less popular approach, that has been suggested in the literature, is to connect the macroscopic droplet bulk with the extending solid surface through a microscopic structure [216], referred to as the interface formation model in later studies [217,218]. The microscopic contact angle, as part of the solution, is determined according to the contact line conditions arising from a local mechanical balance with no assumptions required on its velocity dependence from the experimental results. The interface formation model is more complex compared to the former approach and still holds debates on its physical basis, while the exploration on the microscopic physics, *e.g.* rolling or not, is effort-worthy and most close to a comprehensive mathematical description.

Yet another solution is to assume a microscopic adsorbed film in the dry area on the solid substrate [219], and that the adsorbed film is in thermodynamic equilibrium with both the vapor and solid phases. The existence of the ultrathin adsorbed film, *i.e.* precursor film, has been verified experimentally with the techniques of interference microscopy [220], fluorescence microscopy [221] and atomic force microscopy (AFM) [222], amongst others. Due to the van der Waals effect, equilibrium can be established with non-zero film thickness, thus avoiding the shear-stress singularity at the TPCL. In the simulation of complex multi-component droplets, the assumption of precursor film has been widely utilized [191,192,207,211], which proves to be efficient in accurately predicting the droplet motion without additional empirical correlations. Additionally, the expressions for van der Waals force can be modified for better simulating the actual processes for different surface conditions [223–225]. Readers are referred to the classical review paper by De Gennes [226] and more recently by Bonn et al. [227], as well as the book by Starov and Velarde [228] for more detailed descriptions and summaries of the precursor film theory and the liquid–solid interactions in various processes of wetting and spreading.

5.1.5. Main physical processes and corresponding models

Depending on the dominating mechanisms, the available numerical models can be divided as (1) two-side models which fully account for the transport processes in three phases [17], (2) one-and-half models which treat the process in the gas domain as vapor diffusion, and relate to the liquid phase by concentration balance boundary condition at the gas–liquid interface [188,189], and (3) one-side models [110,192,207] which focus on the physical processes in the liquid phase and derive the evaporation mass flux based on the sticking and departing coefficients of molecules, such as the Hertz–Knudsen equation [229].

The two-side models are suitable for cases in complex situations where the physical processes in all phases need to be considered. In a two-side model, full resolution of both phases requires a complete solution of the continuum, Navier–Stokes, Energy, and concentration equations within the droplet and across the gas domain. This kind of model [17] is able to capture the various effects along with interfacial phase change, such as the natural convection in the gas phase, the vapor recoil near the liquid–gas interface, the complex flow patterns in the liquid phase, and the heat conduction within the solid substrate. One apparent disadvantage of the two-side model is the complexity and the considerable computational cost.

The one-and-half side models simplify the mass transfer at the gas side by ignoring convection, which is reliable especially for droplets in still air where vapor diffusion dominates. In the simulation, the liquid phase is fully solved, while the gas phase is solved merely for diffusion. The two phases are related according to the energy balance and compositional mass balance at the liquid–gas interface. Additionally, the vapor diffusion at the air side can be further simplified by omitting the transient terms according to a steady-state assumption. With this simplification, the diffusion process can be described by a Laplace equation, similar with the electrostatic potential distribution around a spherical-cap-shape conductor, and has been adopted extensively in existing models for droplet evaporation [12,30,188,189].

The one-side models assume the state of the gas phase as homogeneous, vapor diffuses rapidly away from the liquid–gas interface, and the air layer near the droplet interface remains unsaturated. The model can efficiently capture the physical processes inside the droplet, and are especially suitable for non-isothermally heated droplets and multi-component droplets where the thermal transport and solute diffusion in the liquid phase dominate [21,69,99,206,207]. At proper settings, the one-side models are capable to capture the dominating mechanisms with high computational efficiency and modest resources.

On the other hand, depending on the complexity of the target phenomena, the models can also be formulated as full 3D models, 2D models with axial symmetry, and axial symmetric models with the lubrication approximation. In Table 3, we list the dominating physical processes during the evaporation of different type of multi-component droplets. The representative numerical studies are summarized, along with the notions representing the model types (1 side: one-side model; 1.5 side: one-and-half model; 2 side: two-side model; 3D: three dimensional model; 2D: two dimensional axial symmetric model; Lubrication: Lubrication-type model).

Table 3
Main physical processes in the evaporation of different type of multi-component droplets along with the representative numerical work, where the notions in the brackets indicate the model type. 1 side: one-side model; 1.5 side: one-and-half model; 2 side: two-side model; 3D: three dimensional model; 2D: two dimensional axial symmetric model; Lubrication: Lubrication-type model.

Liquid type	Characteristics	Physical processes	Representative numerical work
Binary volatile liquid	Spatial–temporal evolution of mass flux; Liquid properties change as the components vary with time.	Preferential evaporation; solutal Marangoni flow; thermal Marangoni flow; phase segregation; *etc.*	[17] (2 side, 3D); [110] (1 side, Lubrication; [188] (1.5side, Lubrication); [189] (1.5side, 2D); [136] (1.5 side, 3D); [191] (1 side, Lubrication); [174] (2 side, 3D)
Surfactant solution	Surface tension changes drastically with the distribution of surfactant.	Surfactant agglomeration, diffusion and convection; solutal Marangoni flow; super-spreading	[99] (1 side, Lubrication); [207] (1 side, Lubrication); [208] (1 side, Lubrication)
Ionic solution	Solution properties change with salt concentration	Solute diffusion; solutal Marangoni flow; thermal Marangoni flow; crystallization	[147] (1 side, 2D); [148] (1.5 side, 2D); [149] (1.5 side, 2D); [192] (1 side, Lubrication)
Colloidal solution	Colloids deposit along with water evaporation	Capillary flow; particle convection; contact line pinning	[209] (1 side, Lubrication); [210] (1 side, Lubrication); [211] (1 side, Lubrication)

5.2. Empirical models

The fully developed numerical models and analytical solutions such as the one derived by Popov [14] and Stauber [230] provide detailed information of the physical fields in corresponding domains, while in practical situations, general information such as the droplet lifetime is usually needed. In such cases, empirical models based on experimental data provide an efficient way for the prediction of droplet lifetime. To develop an empirical model, the droplet can be considered as fully mixed and the thermophysical properties of the binary liquid are calculated from the properties of individual components along with their compositions. Kita et al. [112] developed an empirical model for evaporating ethanol droplets in a humid environment. As reported earlier, in low humidity environments absorption/adsorption onto an ethanol droplet ensue, while in high humidity environments condensation additionally takes place. In both cases, the droplet transitions into a binary mixture. The empirical model is developed by revisiting the analytical model and equation derived by Popov [14] for the lifetime of pure liquid droplets (see Eqs. (8) and (9), [230]),

$$\frac{\mathrm{d}V}{\mathrm{d}t} = -\frac{\pi D_{12}(T_{\mathrm{amb}})(c_{\mathrm{sat}}(T_{\mathrm{amb}}) - c_\infty)}{\rho} \frac{Rg(\theta)}{(1 + \cos\theta)^2}, \tag{8}$$

$$g(\theta) = (1 + \cos\theta)^2 \left\{ \tan\frac{\theta}{2} + 8 \int_0^\infty \frac{\cosh^2\theta\tau}{\sinh 2\pi\tau} \tanh\left[\tau(\pi - \theta)\right] \mathrm{d}\tau \right\}, \tag{9}$$

which accounts for the change of ethanol concentration (Eq. (5)),

$$\frac{\mathrm{d}V}{\mathrm{d}t} = -\frac{\pi D_{12}(T_{\mathrm{amb}}) c_{\mathrm{sat}}(T_{\mathrm{amb}}) x_{\mathrm{ethanol}}}{\rho} \frac{Rg(\theta)}{(1 + \cos\theta)^2}, \tag{10}$$

the change in the diffusion coefficient function of the relative humidity (Eq. (6)),

$$\frac{\mathrm{d}V}{\mathrm{d}t} = -\frac{\pi D_{12}(T_{\mathrm{amb}}, \mathrm{RH}) c_{\mathrm{sat}}(T_{\mathrm{amb}}) x_{\mathrm{ethanol}}}{\rho} \frac{Rg(\theta)}{(1 + \cos\theta)^2}, \tag{11}$$

and the water intake in time (Eq. (7)), respectively.

$$\frac{\mathrm{d}V}{\mathrm{d}t} = -\frac{\pi D_{12}(T_{\mathrm{amb}}, \mathrm{RH}) c_{\mathrm{sat}}(T_{\mathrm{amb}}) x_{\mathrm{ethanol}}}{\rho} \frac{Rg(\theta)}{(1 + \cos\theta)^2} + \frac{\mathrm{d}x_{\mathrm{water}}}{\mathrm{d}t} V, \tag{12}$$

where $\mathrm{d}V/\mathrm{d}t$ is the change of volume in time or evaporation rate, ρ is the liquid density, c_{sat} and c_∞ are the saturation concentration of ethanol and the concentration of ethanol far away from the droplet ($c_\infty = 0$), D_{12} is the diffusion coefficient of 1 in 2, *i.e.* ethanol in air for this case, and x is the concentration of individual species.

Gurrala et al. [231] decomposed the cause of evaporation flux of a sessile droplet into four effects: (i) the mass flux due to the diffusion of vapor in the ambient air, (ii) the mass flux due to the Stefan flow, (iii) the mass flux due to the free convection of vapor from the saturated interface to the unsaturated ambient, and (iv) the passive mass transport flux due to the natural convection of air from the hot substrate to the cool ambient. Based on the influencing factors of each effect and by reasonably neglecting the Stefan flow effect, they firstly derive an expression for the evaporation rate of pure ethanol from heated substrates as the sum of diffusion (d), convection (c) and passive transport (t) terms,

$$\frac{\mathrm{d}m}{\mathrm{d}t} = \left(\frac{\mathrm{d}m}{\mathrm{d}t}\right)_d + \left(\frac{\mathrm{d}m}{\mathrm{d}t}\right)_c + \left(\frac{\mathrm{d}m}{\mathrm{d}t}\right)_t = h_{\mathrm{d+c}} A_s M \left(c_{\mathrm{sat}}(T_s) - c_\infty(T_\infty)\right) + Y_v^s \left(\frac{\mathrm{d}m}{\mathrm{d}t}\right)_a, \tag{13}$$

where h_{d+c} is the combined diffusion and convection mass transfer coefficient, A_s is the liquid-vapor interface area, M is the molecular weight of the fluid, Y_v^s is the mass fraction of (ethanol) vapor above the free surface of the droplet, and $\left(\frac{dm}{dt}\right)_a$ is the mass convection of air over the area of the heated substrate covered by the droplet, expressed as,

$$\left(\frac{dm}{dt}\right)_a = h_m^a \pi R^2 \frac{M_a}{R_u} \left(\frac{p_\infty^a}{T_\infty} - \frac{p_s^a}{T_s}\right),$$ (14)

where air is approximated as an ideal gas, h_m^a denotes the mass transfer coefficient for air, M_a is the molecular weight of air, R_u is the universal gas constant, p_∞^a and p_s^a are the partial pressures of air at the ambient and near the substrate, respectively. For a binary volatile droplet, they utilize the same expressions for the total evaporation rate. Differently, the vapor pressure of the binary mixture is calculated from the vapor–liquid equilibrium (VLE) diagram for a given mole fraction and substrate temperature. The vapor pressure and vapor phase mixture composition data from the VLE diagram are used to calculate the instantaneous evaporation rate of the individual components. The new molar composition of the liquid in the droplet for the next time step is calculated subsequently and is used in conjunction with the VLE diagram to evaluate the new vapor pressure and the component composition of newly evaporated vapor. This iterative process continues till the end of evaporation. The liquid solution density is evaluated at every time step, which is utilized to evaluate the instantaneous droplet volume.

Ozturk and Erbil [114,232] developed a simplified model for diffusion-limited binary droplet evaporation taking ethanol–water mixture as an example. This binary model is based on the diffusion-limited model for pure liquid droplets derived by Picknett and Bexon [9,233] by analogizing the problem to evaluating the capacitance of an isolated conducting body that is of the same size and shape as the droplet (an equiconvex lens). To extend the approach to binary cases, Ozturk and Erbil accounted for the parameters that characterize the complexity of binary mixtures, including the total vapor pressure, which is obtained by the summation of partial vapor pressures of all components, $P_{v(12)}$; average diffusion coefficient of mixed vapors, $D_{(12)}$; and average bulk liquid density of the drop, $\rho_{(12)}$; and average molecular weight, $M_{(12)}$ of the binary ethanol–water drop. The modified correlation of evaporation rate is expressed as,

$$-\frac{dV^{2/3}}{dt} = \frac{4}{3}\pi \left(\frac{3}{\pi}\right)^{1/3} (D_{12})_t \frac{(M_{12})_t (P_{12})_t (1 - RH)}{R_u T} \frac{(f(\theta))_t}{(P_{12})_t \left(\beta^{1/3}\right)_t},$$ (15)

$$\beta = (1 - \cos\theta)^2 + 2 + \cos\theta$$ (16)

$$f(\theta) = 0.00008957 + 0.6333\theta + 0.116\theta^2 - 0.08878\theta^3 + 0.01033\theta^4$$ (17)

where V is the volume of the binary drop, R_u is the gas constant, T is the temperature, $[P_{v(12)}(1 - RH)]$ is the difference between total vapor pressure of ethanol–water mixture and the water vapor pressure of the ambient far away from the drop. For the calculations, the total vapor pressure can be obtained from the VLE diagram, the liquid density $\rho_{(12)}$ can be retrieved from the literature, the average molecular weight, $M_{(12)}$ is calculated by Dalton's law according to the molar fractions of ethanol in the gas phase, y_{eth}, in equilibrium conditions, and the average diffusion coefficient of the binary mixture can be derived from the molar average of the diffusion coefficients of the components along with its relation with the temperature. Here, $f(\theta)$ is a function of contact angle of the spherical cap. Eq. (17) is an empirical polynomial fit of $f(\theta)$ which indicates the effect of contact angle on the evaporation rate. The authors derived the expressions of these properties for ethanol–water binary mixture. They also summarized parameter tables for specific compositions and temperatures (accounting for the effect of evaporation cooling) so that the evaporation rate can be easily predicted with the modified correlation and by a simple lookup at the summarized tables [114].

The empirical models are simple and convenient for an efficient approximation of the evaporation rate. Note that we refer empirical models to those derived by rectifying the existing theoretical models to accommodate for the experimental results observed. The derived correlations directly reflect the main influence of key factors, *i.e.* contact angle, interfacial and ambient temperature, liquid composition, ambient humidity, *etc.*, on droplet evaporation. Nevertheless, the established empirical models are based on the assumption that the droplet is fully mixed and neglects the concentration gradient and the complex internal flows taking place inside real multicomponent droplets. Therefore, the predicted evaporation rate may derivate from its actual value. Additionally, the distribution of the interfacial mass flux as well as the important physical processes along with droplet evaporation cannot be precisely captured.

6. Conclusions and perspectives

Multicomponent droplets are widely distributed in nature, domestic and industrial fields. They also come with complex physical phenomena of wetting, spreading, phase change, as well as heat and mass transfer between the solid, liquid and gas phases. With increasing research interest, studies on this topic have seen a boost in recent years. The development of new experimental techniques and mathematical models bring new understandings of the underneath physical mechanisms. In this paper, we overview recent progresses in the study of multicomponent droplets. Specifically, we summarize the droplet wetting and phase change dynamics, evaporative mass flux, and flow patterns with different type of multicomponent droplets along with a detailed review of the dominating physical effects. The available experimental and numerical methods are classified, including the application scenarios and measurement accuracy of

different experimental techniques, the governing equations, main assumptions and solutions for complex droplets via mathematical modeling, *etc.*

Compared to single component droplets, the addition of extra components leads to spatiotemporal variation of the interfacial mass fluxes, strong solutal Marangoni flow, Rayleigh flow, as well as other distinguished phenomena including phase separation, emulsification, absorption/adsorption of ambient vapor, *etc.* Studies from many individual groups have revealed that the preferential interfacial phase change and the arising internal flow patterns can be strong enough to induce diverse droplet dynamics and even to drive droplet motion. Investigations into these new phenomena enriches our current knowledge of thermal science and fluid mechanics at the droplet scale. The many recent studies on this topic also evidence the scientific potential for explorations combining experimental observation, theoretical validation, and numerical simulation.

Industrial innovations and more sustainable processes are possible with a better understanding of the fundamental science underlying the phenomena at hand. To this end, for example, in inkjet printing [66] inks are complex mixtures with surfactants, pigments and other additives. These components differ in surface tension, density, viscosity and volatility. In the nozzle part, the preferential evaporation of individual components may change the properties of the remaining ink, causing unstable output of droplet jets and even the nozzle blockage and consequent malfunction. To ensure the optimum and long-term continuous operation, this system requires further systematic investigations. The impact of successive ink drops onto substrates with different permeability, rigidity, roughness or moving velocity is another process worth of extensive exploration, where the spreading, penetration and bouncing of the drops directly affect the printing quality. The final process of ink drying decides the sharpness and clarity of the printing where the selective evaporation of different components and the induced flow affect the pigment depositions. The fine control and optimization of inkjet printing can bring consequent material and energy savings in a wide range of multidisciplinary areas from photography, to MEMS and to electronic circuits, amongst others.

In the pharmaceutical industry, the extraction/nucleation of components due to droplet evaporation or resulting from solvent exchange [43] provides an effective way for the fabrication of multifunctional colloids and drug-loaded microparticles with stable quality and size distribution. The nanoextraction of tracer components by solvent exchange [234] also contributes to the development of nanodroplet-based sensing techniques for quick in-situ diagnosis. In chemical synthesis, droplets can serve as microlabs for chemical reactions, *i.e.*, microreactors, which would otherwise be impossible to achieve in bulk water [235]. This is owed to the existence of an interface which activates the molecules with additional solvation energy due to solubilization.

In biology and cell research, coacervation, the liquid–liquid phase separation in aqueous polyelectrolyte solution, is considered as one main mechanism of the formation of primitive life [236]. In recent years, the coacervation phenomenon of specific proteins is found to play a role in gene silencing, where the sequestration of compacted chromatin in phase-separated droplets of specific proteins may be one decisive mechanism [237,238]. Additionally, as an indication of the state of cells, it exhibits great potential in quick disease diagnosis with a tiny amount of cell samples.

In the semiconductor industry, the cleansing of silicon wafers requires a good manipulation of "Marangoni drying" [239], where the interplay of droplets of cleansing liquids, usually alcohols and additive surfactants, plays a crucial role. In Marangoni drying, special attention is needed on the spatiotemporal variation of surface tensions, where improper manipulation may cause the formation of pollutant stains and sometimes damage the fragile surface structures. Additionally, by properly utilizing the Marangoni effect, contactless digital PCR (polymerase chain reaction) with droplet arrays is possible, which guarantees the purity of the sample and thus the accuracy of the measurement or the analysis.

From the academic perspective, a comprehensive unraveling of the colorful fundamental physics underlying these novel systems is required. On one hand, the internal mechanisms and phenomena playing a role during the evaporation of multi-component droplets are not well-understood and the precise quantification of the dimensionless numbers experimentally via current observation techniques is lacking. Hence, the development of new experimental techniques or coupling of available current ones may further enhance our understanding of the complex mechanisms taking place during binary and multi-component droplet evaporation. On the other hand, the numerical modeling of evaporating multicomponent droplets encounters great challenges, and the difficulty lies in the tracing of the sharp moving interfaces with phase change, in the proper mathematical descriptions of various volatile/nonvolatile components, and in the parallelization of these codes.

On the aspect of droplet operation, the realization of programmed droplet deformation and motion requires a quantitative and systematic evaluation of the droplet behaviors in relation to the characteristics of the origin factors and the strength of the induced flow. Besides, the dynamic structures of contact line and precursor film require further exploration, which is of great importance to predictable control of droplet motion and the precise mathematical modeling.

In terms of flow patterns and droplet dynamics, active control can be realized through different ways: (1) by tentatively designing the structure, wettability and temperature distribution of the underlying surface, *e.g.* with texture contrast or temperature and wettability gradient, (2) by fully taking advantage of the thermophysical properties of multicomponent droplets, *e.g.* droplet motion by self-induced surface tension gradients or density gradients due to preferential evaporation, (3) by tuning the strength and direction of interfacial mass fluxes with external vapor sources, *e.g.* droplets in response to an adjacent droplet or an external vapor source, (4) with the assistance of external physical fields, *e.g.* electric field or magnetic field, *etc.* The controllable flow patterns will subsequently lead to the formation of distinctive patterns as the droplet dries out in the case of colloidal ones, indicating great potentials in high-quality chemical coating, inkjet printing, droplet size chemical reactors, *etc.*

To conclude, within this review, we are highlighting the importance of developing advanced experimental techniques and effective mathematical models for exploring intriguing phenomena and revealing complex mechanisms present within multicomponent droplets. Especially, with the application of high-resolution and high-speed microscopy, which was initially utilized in the biological field, it has been possible to trace the evolution of fluid structures with exclusive detail. The increasing computation capacity nowadays also makes it possible to reach the real picture of a practical process by modeling the many interacting physical processes with minimal assumptions and simplifications. To meet the challenge both in academic research and in industrial applications, intensified interdisciplinary and multidisciplinary communication and synergistic cooperation are highly needed. These require the close interaction and communication from fluid mechanics and thermal science with biological technology, material science, chemical physics, atmospheric science and other engineering disciplines. As academic research in all disciplinaries goes forward, new findings are expected with the rising up of new questions and challenges. More importantly, studies on multicomponent droplets should go with the demand of cutting-edge technologies, which may bring renewed vigor to this traditional research field and at the same time cultivate new progresses in the fundamental science.

Declaration of competing interest

The authors declare that they have no known competing financial interests or personal relationships that could have appeared to influence the work reported in this paper.

Acknowledgments

References

[1] M. Singh, H.M. Haverinen, P. Dhagat, G.E. Jabbour, Inkjet printing—process and its applications, Adv. Mater. 22 (6) (2010) 673–685.
[2] J. Kim, Spray cooling heat transfer: The state of the art, Int. J. Heat Fluid Flow 28 (4) (2007) 753–767.
[3] C.J. Brinker, Y. Lu, A. Sellinger, H. Fan, Evaporation-induced self-assembly: nanostructures made easy, Adv. Mater. 11 (7) (1999) 579–585.
[4] W. Wang, J. Lin, D.C. Schwartz, Scanning force microscopy of DNA molecules elongated by convective fluid flow in an evaporating droplet, Biophys. J. 75 (1) (1998) 513–520.
[5] J.L. Garcia-Cordero, Z.H. Fan, Sessile droplets for chemical and biological assays, Lab A Chip 17 (13) (2017) 2150–2166.
[6] J.C. Maxwell, in: W.D. Niven (Ed.), Scientific Papers, Vol. 2, Cambridge, 1890.
[7] I. Langmuir, The evaporation of small spheres, Phys. Rev. 12 (5) (1918) 368.
[8] A. Fick, Ueber diffusion, Ann. Phys. 170 (1) (1855) 59–86.
[9] R.G. Picknett, R. Bexon, The evaporation of sessile or pendant drops in still air, J. Colloid Interface Sci. 61 (2) (1977) 336–350.
[10] R.D. Deegan, O. Bakajin, T.F. Dupont, G. Huber, S.R. Nagel, T.A. Witten, Capillary flow as the cause of ring stains from dried liquid drops, Nature 389 (6653) (1997) 827.
[11] R.D. Deegan, O. Bakajin, T.F. Dupont, G. Huber, S.R. Nagel, T.A. Witten, Contact line deposits in an evaporating drop, Phys. Rev. E 62 (1) (2000) 756.
[12] R.D. Deegan, Pattern formation in drying drops, Phys. Rev. E 61 (1) (2000) 475.
[13] H. Hu, R.G. Larson, Evaporation of a sessile droplet on a substrate, J. Phys. Chem. B 106 (6) (2002) 1334–1344.
[14] Y.O. Popov, Evaporative deposition patterns: spatial dimensions of the deposit, Phys. Rev. E 71 (3) (2005) 036313.
[15] W. Ramsay, The Life and Letters of Joseph Black, MD. Constable, 1918.
[16] K. Sefiane, R. Bennacer, An expression for droplet evaporation incorporating thermal effects, J. Fluid Mech. 667 (2011) 260–271.
[17] P.J. Sáenz, K. Sefiane, J. Kim, O.K. Matar, P. Valluri, Evaporation of sessile drops: a three-dimensional approach, J. Fluid Mech. 772 (2015) 705–739.
[18] K. Sefiane, J.R. Moffat, O.K. Matar, R.V. Craster, Self-excited hydrothermal waves in evaporating sessile drops, Appl. Phys. Lett. 93 (7) (2008) 074103.
[19] H. Hu, R.G. Larson, Analysis of the effects of marangoni stresses on the microflow in an evaporating sessile droplet, Langmuir 21 (9) (2005) 3972–3980.
[20] H. Hu, R.G. Larson, Marangoni effect reverses coffee-ring depositions, J. Phys. Chem. B 110 (14) (2006) 7090–7094.
[21] G. Karapetsas, O.K. Matar, P. Valluri, K. Sefiane, Convective rolls and hydrothermal waves in evaporating sessile drops, Langmuir 28 (31) (2012) 11433–11439.
[22] M. Ma, R.M. Hill, Superhydrophobic surfaces, Curr. Opin. Colloid Interface Sci. 11 (4) (2006) 193–202.
[23] L.H. Tanner, The spreading of silicone oil drops on horizontal surfaces, J. Phys. D: Appl. Phys. 12 (9) (1979) 1473.
[24] G. McHale, S. Aqil, N.J. Shirtcliffe, M.I. Newton, H.Y. Erbil, Analysis of droplet evaporation on a superhydrophobic surface, Langmuir 21 (24) (2005) 11053–11060.
[25] H. Gelderblom, A.G. Marin, H. Nair, A. Van Houselt, L. Lefferts, J.H. Snoeijer, D. Lohse, How water droplets evaporate on a superhydrophobic substrate, Phys. Rev. E 83 (2) (2011) 026306.
[26] D. Tam, V. von Arnim, G.H. McKinley, A.E. Hosoi, Marangoni convection in droplets on superhydrophobic surfaces, J. Fluid Mech. 624 (2009) 101–123.

[27] S. Dash, S.V. Garimella, Droplet evaporation dynamics on a superhydrophobic surface with negligible hysteresis, Langmuir 29 (34) (2013) 10785–10795.

[28] D. Orejon, K. Sefiane, M.E. Shanahan, Stick–slip of evaporating droplets: substrate hydrophobicity and nanoparticle concentration, Langmuir 27 (21) (2011) 12834–12843.

[29] J.R. Moffat, K. Sefiane, M.E. Shanahan, Effect of TiO$_2$ nanoparticles on contact line stick- slip behavior of volatile drops, J. Phys. Chem. B 113 (26) (2009) 8860–8866.

[30] G.J. Dunn, S.K. Wilson, B.R. Duffy, S. David, K. Sefiane, The strong influence of substrate conductivity on droplet evaporation, J. Fluid Mech. 623 (2009) 329–351.

[31] B. Sobac, D. Brutin, Thermal effects of the substrate on water droplet evaporation, Phys. Rev. E 86 (2) (2012) 021602.

[32] K. Sefiane, R. Bennacer, An expression for droplet evaporation incorporating thermal effects, J. Fluid Mech. 667 (2011) 260–271.

[33] S. David, K. Sefiane, L. Tadrist, Experimental investigation of the effect of thermal properties of the substrate in the wetting and evaporation of sessile drops, Colloids Surf. A 298 (1–2) (2007) 108–114.

[34] W.D. Ristenpart, P.G. Kim, C. Domingues, J. Wan, H.A. Stone, Influence of substrate conductivity on circulation reversal in evaporating drops, Phys. Rev. Lett. 99 (23) (2007) 234502.

[35] F. Carle, B. Sobac, D. Brutin, Experimental evidence of the atmospheric convective transport contribution to sessile droplet evaporation, Appl. Phys. Lett. 102 (6) (2013) 061603.

[36] K. Sefiane, S.K. Wilson, S. David, G.J. Dunn, B.R. Duffy, On the effect of the atmosphere on the evaporation of sessile droplets of water, Phys. Fluids 21 (6) (2009) 062101.

[37] D. Orejon, M.E. Shanahan, Y. Takata, K. Sefiane, Kinetics of evaporation of pinned nanofluid volatile droplets at subatmospheric pressures, Langmuir 32 (23) (2016) 5812–5820.

[38] E. Dietrich, M. Rump, P. Lv, E.S. Kooij, H.J. Zandvliet, D. Lohse, Segregation in dissolving binary-component sessile droplets, J. Fluid Mech. 812 (2017) 349–369.

[39] Y. Li, P. Lv, C. Diddens, H. Tan, H. Wijshoff, M. Versluis, D. Lohse, Evaporation-triggered segregation of sessile binary droplets, Phys. Rev. Lett. 120 (22) (2018) 224501.

[40] H. Kim, H.A. Stone, Direct measurement of selective evaporation of binary mixture droplets by dissolving materials, J. Fluid Mech. 850 (2018) 769–783.

[41] L. Keiser, H. Bense, P. Colinet, J. Bico, E. Reyssat, Marangoni bursting: evaporation-induced emulsification of binary mixtures on a liquid layer, Phys. Rev. Lett. 118 (7) (2017) 074504.

[42] G. Durey, H. Kwon, Q. Magdelaine, M. Casiulis, J. Mazet, L. Keiser, et al., Marangoni bursting: Evaporation-induced emulsification of a two-component droplet, Phys. Rev. Fluids 3 (10) (2018) 100501.

[43] S.A. Vitale, J.L. Katz, Liquid droplet dispersions formed by homogeneous liquid- liquid nucleation: The ouzo effect, Langmuir 19 (10) (2003) 4105–4110.

[44] H. Tan, C. Diddens, P. Lv, J.G.M. Kuerten, X. Zhang, D. Lohse, Evaporation-triggered microdroplet nucleation and the four life phases of an evaporating Ouzo drop, Proc. Natl. Acad. Sci. 113 (31) (2016) 8642–8647.

[45] H. Tan, S. Wooh, H.J. Butt, X. Zhang, D. Lohse, Porous supraparticle assembly through self-lubricating evaporating colloidal ouzo drops, Nature Commun. 10 (1) (2019) 478.

[46] P. Zhu, T. Kong, C. Zhou, L. Lei, L. Wang, Engineering microstructure with evaporation-induced self-assembly of microdroplets, Small Methods 2 (6) (2018) 1800017.

[47] A.M.J. Edwards, P.S. Atkinson, C.S. Cheung, H. Liang, D.J. Fairhurst, F.F. Ouali, Density-driven flows in evaporating binary liquid droplets, Phys. Rev. Lett. 121 (18) (2018) 184501.

[48] Y. Li, C. Diddens, P. Lv, H. Wijshoff, M. Versluis, D. Lohse, Gravitational effect in evaporating binary microdroplets, Phys. Rev. Lett. 122 (11) (2019) 114501.

[49] M. Pasandideh-Fard, Y.M. Qiao, S. Chandra, J. Mostaghimi, Capillary effects during droplet impact on a solid surface, Phys. Fluids 8 (3) (1996) 650–659.

[50] A. Rachih, D. Legendre, E. Climent, S. Charton, Numerical study of conjugate mass transfer from a spherical droplet at moderate Reynolds number, Int. J. Heat Mass Transfer 157 (2020) 119958.

[51] M. Renksizbulut, M. Bussmann, Multicomponent droplet evaporation at intermediate Reynolds numbers, Int. J. Heat Mass Transfer 36 (11) (1993) 2827–2835.

[52] V. Vaikuntanathan, D. Sivakumar, Maximum spreading of liquid drops impacting on groove-textured surfaces: effect of surface texture, Langmuir 32 (10) (2016) 2399–2409.

[53] J.B. Boreyko, C.P. Collier, Dewetting transitions on superhydrophobic surfaces: When are Wenzel drops reversible? J. Phys. Chem. C 117 (35) (2013) 18084–18090.

[54] P.G. De Gennes, Wetting: statics and dynamics, Rev. Modern Phys. 57 (3) (1985) 827.

[55] D. Bonn, J. Eggers, J. Indekeu, J. Meunier, E. Rolley, Wetting and spreading, Rev. Modern Phys. 81 (2) (2009) 739.

[56] R.V. Craster, O.K. Matar, Dynamics and stability of thin liquid films, Rev. Modern Phys. 81 (3) (2009) 1131.

[57] D. Brutin, V. Starov, Recent advances in droplet wetting and evaporation, Chem. Soc. Rev. 47 (2) (2018) 558–585.

[58] H.Y. Erbil, Evaporation of pure liquid sessile and spherical suspended drops: A review, Adv. Colloid Interface Sci. 170 (1–2) (2012) 67–86.

[59] A.M. Cazabat, G. Guena, Evaporation of macroscopic sessile droplets, Soft Matter 6 (12) (2010) 2591–2612.

[60] M.E. Cates, E. Tjhung, Theories of binary fluid mixtures: from phase-separation kinetics to active emulsions, J. Fluid Mech. 836 (2018).

[61] K. Sefiane, Patterns from drying drops, Adv. Colloid Interface Sci. 206 (2014) 372–381.

[62] C.C. Maass, C. Krüger, S. Herminghaus, C. Bahr, Swimming droplets, Annu. Rev. Condens. Matter Phys. 7 (2016) 171–193.

[63] D. Lohse, X. Zhang, Surface nanobubbles and nanodroplets, Rev. Modern Phys. 87 (3) (2015) 981.

[64] H. Manikantan, T.M. Squires, Phoretic self-propulsion, Annu. Rev. Fluid Mech. 49 (2017) 511–540.

[65] Harishankar Manikantan, Todd M. Squires, Surfactant dynamics: hidden variables controlling fluid flows, J. Fluid Mech. 892 (2020).

[66] D. Lohse, Fundamental fluid dynamics challenges in inkjet printing, Annu. Rev. Fluid Mech. 54 (2022) 1.

[67] D. Lohse, X. Zhang, Physicochemical hydrodynamics of droplets out of equilibrium, Nat. Rev. Phys. 2 (8) (2020) 426–443.

[68] T. Young, Philos. Trans. R. Soc. (London) 95 (1805) 65–87.

[69] D.M. Anderson, S.H. Davis, The spreading of volatile liquid droplets on heated surfaces, Phys. Fluids 7 (2) (1995) 248–265.

[70] V.S. Ajaev, Spreading of thin volatile liquid droplets on uniformly heated surfaces, J. Fluid Mech. 528 (2005) 279–296.

[71] A.A. Pahlavan, L. Yang, C.D. Bain, H.A. Stone, Evaporation of binary-mixture liquid droplets: The formation of picoliter pancakelike shapes, Phys. Rev. Lett. 127 (2) (2021) 024501.

[72] V. Kubyshkina, D. Orejon, C.M. Dover, K. Sefiane, Geometrical deposits on microstructured surfaces, J. Bionic Eng. 17 (4) (2020) 851–865.

[73] K.M. Al Balushi, K. Sefiane, D. Orejon, Binary mixture droplet wetting on micro-structure decorated surfaces, J. Colloids Interface Sci. 612 (2022) 792–805.

[74] X. Fanton, A.M. Cazabat, Spreading and instabilities induced by a solutal marangoni effect, Langmuir 14 (9) (1998) 2554–2561.

[75] J.F. Hernández-Sánchez, A. Eddi, J.H. Snoeijer, Marangoni spreading due to a localized alcohol supply on a thin water film, Phys. Fluids 27 (3) (2015) 032003.

[76] D. Pesach, A. Marmur, Marangoni effects in the spreading of liquid mixtures on a solid, Langmuir 3 (4) (1987) 519–524.

[77] M.E. Shanahan, K. Sefiane, Recalcitrant bubbles, Sci. Rep. 4 (1) (2014) 1–9.

[78] N.J. Cira, A. Benusiglio, M. Prakash, Vapour-mediated sensing and motility in two-component droplets, Nature 519 (7544) (2015) 446.

[79] S. Karpitschka, F. Liebig, H. Riegler, Marangoni contraction of evaporating sessile droplets of binary mixtures, Langmuir 33 (19) (2017) 4682–4687.

[80] M.A. Hack, W. Kwieciński, O. Ramírez-Soto, T. Segers, S. Karpitschka, E.S. Kooij, J.H. Snoeijer, Wetting of two-component drops: Marangoni contraction versus autophobing, Langmuir 37 (12) (2021) 3605–3611.

[81] Y. Abe, Self-rewetting fluids: Beneficial aqueous solutions, Ann. New York Acad. Sci. 1077 (1) (2006) 650–667.

[82] Y. Hu, K. Huang, J. Huang, A review of boiling heat transfer and heat pipes behaviour with self-rewetting fluids, Int. J. Heat Mass Transfer 121 (2018) 107–118.

[83] R. Vochten, G. Pétré, R. Defay, Study of the heat of reversible adsorption at the air-solution interface, I. Thermodynamical calculation of the heat of reversible adsorption of nonionic surfactants, J. Colloid Interface Sci. 42 (2) (1973) 310–319.

[84] G. Karapetsas, K.C. Sahu, K. Sefiane, O.K. Matar, Thermocapillary-driven motion of a sessile drop: effect of non-monotonic dependence of surface tension on temperature, Langmuir 30 (15) (2014) 4310–4321.

[85] D. Mamalis, V. Koutsos, K. Sefiane, On the motion of a sessile drop on an incline: Effect of non-monotonic thermocapillary stresses, Appl. Phys. Lett. 109 (23) (2016) 231601.

[86] N. Zhang, Innovative heat pipe systems using a new working fluid, Int. Commun. Heat Mass Transfer 28 (8) (2001) 1025–1033.

[87] R. Savino, A. Cecere, R. Di Paola, Surface tension-driven flow in wickless heat pipes with self-rewetting fluids, Int. J. Heat Fluid Flow 30 (2) (2009) 380–388.

[88] D. Mamalis, V. Koutsos, K. Sefiane, Nonisothermal spreading dynamics of self-rewetting droplets, Langmuir 34 (5) (2018) 1916–1931.

[89] D. Baumgartner, S. Sinha, N. Cira, Spreading and contracting three-component droplets for cleaning high energy surfaces, in: APS Meeting Abstracts, 2019.

[90] D. Myers, Surfactant Science and Technology, third ed., John Wiley & Sons, 2006.

[91] P. Somasundaran, S. Krishnakumar, Adsorption of surfactants and polymers at the solid–liquid interface, Colloids Surf. A 123 (1997) 491–513.

[92] O.K. Matar, R.V. Craster, Dynamics of surfactant-assisted spreading, Soft Matter 5 (20) (2009) 3801–3809.

[93] A.B. Afsar-Siddiqui, P.F. Luckham, O.K. Matar, Unstable spreading of aqueous anionic surfactant solutions on liquid films. 2. Highly soluble surfactant, Langmuir 19 (3) (2003) 703–708.

[94] O.E. Jensen, J.B. Grotberg, Insoluble surfactant spreading on a thin viscous film: shock evolution and film rupture, J. Fluid Mech. 240 (1992) 259–288.

[95] A.D. Dussaud, O.K. Matar, S.M. Troian, Spreading characteristics of an insoluble surfactant film on a thin liquid layer: comparison between theory and experiment, J. Fluid Mech. 544 (2005) 23–51.

[96] K.S. Lee, V.M. Starov, Spreading of surfactant solutions over thin aqueous layers at low concentrations: Influence of solubility, J. Colloid Interface Sci. 329 (2) (2009) 361–365.

[97] P.E. Theodorakis, E.A. Müller, R.V. Craster, O.K. Matar, Superspreading: Mechanisms and molecular design, Langmuir 31 (8) (2015) 2304–2309.

[98] T. Stoebe, Z. Lin, R.M. Hill, M.D. Ward, H.T. Davis, Surfactant-enhanced spreading, Langmuir 12 (2) (1996) 337–344.

[99] G. Karapetsas, R.V. Craster, O.K. Matar, On surfactant-enhanced spreading and superspreading of liquid drops on solid surfaces, J. Fluid Mech. 670 (2011) 5–37.

[100] P.E. Theodorakis, E.A. Müller, R.V. Craster, O.K. Matar, Modelling the superspreading of surfactant-laden droplets with computer simulation, Soft Matter 11 (48) (2015) 9254–9261.

[101] N.N. Lebedev, Special Functions and their Applications, Prentice-Hall, 1965.

[102] K.S. Birdi, D.T. Vu, A. Winter, A study of the evaporation rates of small water drops placed on a solid surface, J. Phys. Chem. 93 (9) (1989) 3702–3703.

[103] K. Sefiane, L. Tadrist, M. Douglas, Experimental study of evaporating water–ethanol mixture sessile drop: influence of concentration, Int. J. Heat Mass Transfer 46 (23) (2003) 4527–4534.

[104] K. Sefiane, On the dynamic capillary effects in the wetting and evaporation process of binary droplets, Fluid Dyn. Mater. Process. 1 (3) (2005) 267–276.

[105] C.H. Ooi, E. Bormashenko, A.V. Nguyen, G.M. Evans, D.V. Dao, N.T. Nguyen, Evaporation of ethanol–water binary mixture sessile liquid marbles, Langmuir 32 (24) (2016) 6097–6104.

[106] K. Sefiane, S. David, M.E. Shanahan, Wetting and evaporation of binary mixture drops, J. Phys. Chem. B 112 (36) (2008) 11317–11323.

[107] C. Liu, E. Bonaccurso, H.J. Butt, Evaporation of sessile water/ethanol drops in a controlled environment, Phys. Chem. Chem. Phys. 10 (47) (2008) 7150–7157.

[108] Y. Yonemoto, T. Kunugi, Experimental and theoretical investigation of contact-angle variation for water–ethanol mixture droplets on a low-surface-energy solid, Int. J. Heat Mass Transfer 96 (2016) 614–626.

[109] C.H. Jeong, H.J. Lee, D.Y. Kim, S.B. Ahangar, C.K. Choi, S.H. Lee, Quantitative analysis of contact line behaviors of evaporating binary mixture droplets using surface plasmon resonance imaging, Int. J. Heat Mass Transfer 165 (2021) 120690.

[110] A.G.L. Williams, G. Karapetsas, D. Mamalis, K. Sefiane, O.K. Matar, P. Valluri, Spreading and retraction dynamics of sessile evaporating droplets comprising volatile binary mixtures, J. Fluid Mech. 907 (2021) A22.

[111] P. Katre, P. Gurrala, S. Balusamy, S. Banerjee, K.C. Sahu, Evaporation of sessile ethanol-water droplets on a critically inclined heated surface, Int. J. Multiph. Flow. 131 (2020) 103368.

[112] Y. Kita, Y. Okauchi, Y. Fukatani, D. Orejon, M. Kohno, Y. Takata, K. Sefiane, Quantifying vapor transfer into evaporating ethanol drops in a humid atmosphere, Phys. Chem. Chem. Phys. 20 (29) (2018) 19430–19440.

[113] Y. Fukatani, D. Orejon, Y. Kita, Y. Takata, J. Kim, K. Sefiane, Effect of ambient temperature and relative humidity on interfacial temperature during early stages of drop evaporation, Phys. Rev. E 93 (4) (2016) 043103.

[114] T. Ozturk, H.Y. Erbil, A simple model for diffusion limited drop evaporation of binary liquids from physical properties of the components: Ethanol-water example, Langmuir (2020).

[115] V. Soulié, S. Karpitschka, F. Lequien, P. Prené, T. Zemb, H. Moehwald, H. Riegler, The evaporation behavior of sessile droplets from aqueous saline solutions, Phys. Chem. Chem. Phys. 17 (34) (2015) 22296–22303.

[116] G.V. Kuznetsov, D.V. Feoktistov, E.G. Orlova, S.Y. Misyura, V.S. Morozov, A.G. Islamova, Evaporation modes of LiBr, CaCl$_2$, LiCl, NaCl aqueous salt solution droplets on aluminum surface, Int. J. Heat Mass Transfer 126 (2018) 161–168.

[117] X. Zhong, J. Ren, F. Duan, Wettability effect on evaporation dynamics and crystalline patterns of sessile saline droplets, J. Phys. Chem. B 121 (33) (2017) 7924–7933.

[118] N. Shahidzadeh-Bonn, S. Rafaï, D. Bonn, G. Wegdam, Salt crystallization during evaporation: impact of interfacial properties, Langmuir 24 (16) (2008) 8599–8605.

[119] N. Shahidzadeh, M.F. Schut, J. Desarnaud, M. Prat, D. Bonn, Salt stains from evaporating droplets, Sci. Rep. 5 (2015) 10335.
[120] S.Y. Misyura, Evaporation and heat transfer of aqueous salt solutions during crystallization, Appl. Therm. Eng. 139 (2018) 203–212.
[121] D. Kaya, V.A. Belyi, M. Muthukumar, Pattern formation in drying droplets of polyelectrolyte and salt, J. Chem. Phys. 133 (11) (2010) 114905.
[122] G. Brenn, Concentration fields in evaporating droplets, Int. J. Heat Mass Transfer 48 (2) (2005) 395–402.
[123] G. Brenn, L.J. Deviprasath, F. Durst, C. Fink, Evaporation of acoustically levitated multi-component liquid droplets, Int. J. Heat Mass Transfer 50 (25-26) (2007) 5073–5086.
[124] I.G. Gusev, P.A. Krutitskii, S.S. Sazhin, A.E. Elwardany, New solutions to the species diffusion equation inside droplets in the presence of the moving boundary, Int. J. Heat Mass Transfer 55 (7-8) (2012) 2014–2021.
[125] V. Jaiswal, A.R. Harikrishnan, G. Khurana, P. Dhar, Ionic solubility and solutal advection governed augmented evaporation kinetics of salt solution pendant droplets, Phys. Fluids 30 (1) (2018) 012113.
[126] Z. Wang, D. Orejon, K. Sefiane, Y. Takata, Water vapor uptake into hygroscopic lithium bromide desiccant droplets: mechanisms of droplet growth and spreading, Phys. Chem. Chem. Phys. 21 (3) (2019) 1046–1058.
[127] Z. Wang, D. Orejon, K. Sefiane, Y. Takata, Coupled thermal transport and mass diffusion during vapor absorption into hygroscopic liquid desiccant droplets, Int. J. Heat Mass Transfer 134 (2019) 1014–1023.
[128] Z. Wang, D. Orejon, K. Sefiane, Y. Takata, Effect of substrate conductivity on the transient thermal transport of hygroscopic droplets during vapor absorption, Micromachines 11 (2) (2020) 193.
[129] S.Y. Misyura, Non-isothermal evaporation in a sessile droplet of water-salt solution, Int. J. Therm. Sci. 124 (2018) 76–84.
[130] S.Y. Misyura, Evaporation of a sessile water drop and a drop of aqueous salt solution, Sci. Rep. 7 (1) (2017) 14759.
[131] X. Xu, J. Luo, Marangoni flow in an evaporating water droplet, Appl. Phys. Lett. 91 (12) (2007) 124102.
[132] J.R. Christy, K. Sefiane, E. Munro, A study of the velocity field during evaporation of sessile water and water/ethanol drops, J. Bionic Eng. 7 (4) (2010) 321–328.
[133] A.G. Marin, H. Gelderblom, D. Lohse, J.H. Snoeijer, Order-to-disorder transition in ring-shaped colloidal stains, Phys. Rev. Lett. 107 (8) (2011) 085502.
[134] Y. Hamamoto, J.R. Christy, K. Sefiane, Order-of-magnitude increase in flow velocity driven by mass conservation during the evaporation of sessile drops, Phys. Rev. E 83 (5) (2011) 051602.
[135] P. Katre, S. Balusamy, S. Banerjee, L.D. Chandrala, K.C. Sahu, Evaporation dynamics of a sessile droplet of binary mixture laden with nanoparticles, Langmuir (2021).
[136] C. Diddens, H. Tan, P. Lv, M. Versluis, J.G.M. Kuerten, X. Zhang, D. Lohse, Evaporating pure, binary and ternary droplets: thermal effects and axial symmetry breaking, J. Fluid Mech. 823 (2017) 470–497.
[137] J.R. Christy, Y. Hamamoto, K. Sefiane, Flow transition within an evaporating binary mixture sessile drop, Phys. Rev. Lett. 106 (20) (2011) 205701.
[138] R. Bennacer, K. Vortices Sefiane, Dissipation and flow transition in volatile binary drops, J. Fluid Mech. 749 (2014) 649–665.
[139] M.A. Jabal, E. Homede, A. Zigelman, O. Manor, Coupling between wetting dynamics, marangoni vortices, and localized hot cells in drops of volatile binary solutions, J. Colloid Interface Sci. (2020).
[140] C. Diddens, Y. Li, D. Lohse, Competing Marangoni and Rayleigh convection in evaporating binary droplets, J. Fluid Mech. 914 (2021).
[141] Y. Li, C. Diddens, T. Segers, H. Wijshoff, M. Verluis, D. Lohse, Rayleigh–staylor instability by segregation in an evaporating multicomponent microdroplet, J. Fluid Mech. 899 (2020) A22.
[142] H. Sadafi, R. Rabani, S. Dehaeck, H. Machrafi, B. Haut, P. Dauby, P. Colinet, Evaporation induced demixing in binary sessile drops, Colloids Surf. A 602 (2020) 125052.
[143] H. Kim, F. Boulogne, E. Um, I. Jacobi, E. Button, H.A. Stone, Controlled uniform coating from the interplay of Marangoni flows and surface-adsorbed macromolecules, Phys. Rev. Lett. 116 (12) (2016) 124501.
[144] H. Tan, C. Diddens, M. Versluis, H.J. Butt, D. Lohse, X. Zhang, Self-wrapping of an ouzo drop induced by evaporation on a superamphiphobic surface, Soft Matter 13 (15) (2017) 2749–2759.
[145] Y. Li, C. Diddens, T. Segers, H. Wijshoff, M. Versluis, D. Lohse, Evaporating droplets on oil-wetted surfaces: Suppression of the coffee-stain effect, Proc. Natl. Acad. Sci. 117 (29) (2020) 16756–16763.
[146] R. Savino, R. Monti, Buoyancy and surface-tension-driven convection in hanging-drop protein crystallizer, J. Cryst. Growth 165 (3) (1996) 308–318.
[147] K.H. Kang, H.C. Lim, H.W. Lee, S.J. Lee, Evaporation-induced saline Rayleigh convection inside a colloidal droplet, Phys. Fluids 25 (4) (2013) 042001.
[148] T.K. Pradhan, P.K. Panigrahi, Influence of an adjacent droplet on fluid convection inside an evaporating droplet of binary mixture, Colloids Surf. A 500 (2016) 154–165.
[149] T.K. Pradhan, P.K. Panigrahi, Evaporation induced natural convection inside a droplet of aqueous solution placed on a superhydrophobic surface, Colloids Surf. A 530 (2017) 1–12.
[150] M. Efstratiou, J. Christy, K. Sefiane, Crystallization-driven flows within evaporating aqueous saline droplets, Langmuir 36 (18) (2020) 4995–5002.
[151] A. Marin, S. Karpitschka, D. Noguera-Marín, M.A. Cabrerizo-Vílchez, M. Rossi, C.J. Kähler, M.A.R. Valverde, Solutal marangoni flow as the cause of ring stains from drying salty colloidal drops, Phys. Rev. Fluids 4 (4) (2019) 041601.
[152] A.M. Lacasta, I.M. Sokolov, J.M. Sancho, F. Sagués, Competitive evaporation in arrays of droplets, Phys. Rev. E 57 (5) (1998) 6198.
[153] C. Schäfle, C. Bechinger, B. Rinn, C. David, P. Leiderer, Cooperative evaporation in ordered arrays of volatile droplets, Phys. Rev. Lett. 83 (25) (1999) 5302.
[154] A.J.D. Shaikeea, S. Basu, Insight into the evaporation dynamics of a pair of sessile droplets on a hydrophobic substrate, Langmuir 32 (5) (2016) 1309–1318.
[155] A. Shaikeea, S. Basu, S. Hatte, L. Bansal, Insights into vapor-mediated interactions in a nanocolloidal droplet system: evaporation dynamics and affects on self-assembly topologies on macro-to microscales, Langmuir 32 (40) (2016) 10334–10343.
[156] H. Sadafi, S. Dehaeck, A. Rednikov, P. Colinet, Vapor-mediated versus substrate-mediated interactions between volatile droplets, Langmuir 35 (21) (2019) 7060–7065.
[157] D. Khilifi, W. Foudhil, K. Fahem, S. Harmand, J.S. Ben, Study of the phenomenon of the interaction between sessile drops during evaporation, Therm. Sci. 23 (2 Part B) (2019) 1105–1114.
[158] A.W. Wray, B.R. Duffy, S.K. Wilson, Competitive evaporation of multiple sessile droplets, J. Fluid Mech. 884 (2020).
[159] J. Wang, X. Huang, X. Qiao, D. Ju, C. Sun, Experimental study on evaporation characteristics of single and multiple fuel droplets, J. Energy Inst. (2020).
[160] K.L. Chong, Y. Li, C.S. Ng, R. Verzicco, D. Lohse, Convection-dominated dissolution for single and multiple immersed sessile droplets, J. Fluid Mech. 892 (2020).
[161] B. Majhy, A.K. Sen, Evaporation-induced transport of a pure aqueous droplet by an aqueous mixture droplet, Phys. Fluids 32 (3) (2020) 032003.
[162] Y. Wen, P.Y. Kim, S. Shi, D. Wang, X. Man, M. Doi, T.P. Russell, Vapor-induced motion of two pure liquid droplets, Soft Matter 15 (10) (2019) 2135–2139.

[163] T.K. Pradhan, P.K. Panigrahi, Influence of an adjacent droplet on fluid convection inside an evaporating droplet of binary mixture, Colloids Surf. A 500 (2016) 154–165.
[164] X. Man, M. Doi, Vapor-induced motion of liquid droplets on an inert substrate, Phys. Rev. Lett. 119 (4) (2017) 044502.
[165] T.K. Pradhan, P.K. Panigrahi, Deposition pattern of interacting droplets, Colloids Surf. A 482 (2015) 562–567.
[166] T.K. Pradhan, P.K. Panigrahi, Vapor mediated interaction of two condensing droplets, Colloids Surf. A 608 (2021) 125555.
[167] P. Kabi, R. Pal, S. Basu, Moses effect: Splitting a sessile droplet using a vapor-mediated marangoni effect leading to designer surface patterns, Langmuir 36 (5) (2020) 1279–1287.
[168] S. Kim, J. Kim, H.Y. Kim, Formation, growth, and saturation of dry holes in thick liquid films under vapor-mediated Marangoni effect, Phys. Fluids 31 (11) (2019) 112105.
[169] S. Kim, J. Kim, H.Y. Kim, Dewetting of liquid film via vapour-mediated smarangoni effect, J. Fluid Mech. 872 (2019) 100–114.
[170] R. Malinowski, I.P. Parkin, G. Volpe, Nonmonotonic contactless manipulation of binary droplets via sensing of localized vapor sources on pristine substrates, Sci. Adv. 6 (40) (2020) eaba3636.
[171] O. Hegde, S. Chakraborty, P. Kabi, S. Basu, Vapor mediated control of microscale flow in sessile droplets, Phys. Fluids 30 (12) (2018) 122103.
[172] R. Malinowski, G. Volpe, I.P. Parkin, G. Volpe, Dynamic control of particle deposition in evaporating droplets by an external point source of vapor, J. Phys. Chem. Lett. 9 (3) (2018) 659–664.
[173] J. Park, J. Ryu, H.J. Sung, H. Kim, Control of solutal marangoni-driven vortical flows and enhancement of mixing efficiency, J. Colloid Interface Sci. 561 (2020) 408–415.
[174] P.J. Sáenz, A.W. Wray, Z. Che, O.K. Matar, P. Valluri, J. Kim, K. Sefiane, Dynamics and universal scaling law in geometrically-controlled sessile drop evaporation, Nature Commun. 8 (2017) 14783.
[175] https://www.infratec-infrared.com/thermography/infrared-camera/imageir-9400/.
[176] https://www.seika-di.com/en/measurement/principle_of_piv/micro_piv_lif.html.
[177] L. Venkatakrishnan, G.E.A. Meier, Density measurements using the background oriented schlieren technique, Exp. Fluids 37 (2) (2004) 237–247.
[178] R. Gupta, C. Das, A. Datta, R. Ganguly, Background oriented Schlieren (BOS) imaging of condensation from humid air on wettability-engineered surfaces, Exp. Therm Fluid Sci. 109 (2019) 109859.
[179] P.L. Kelly-Zion, C.J. Pursell, N. Hasbamrer, B. Cardozo, K. Gaughan, K. Nickels, Vapor distribution above an evaporating sessile drop, Int. J. Heat Mass Transfer 65 (2013) 165–172.
[180] J. Hinrichs, V. Shastry, M. Junk, Y. Hemberger, H. Pitsch, An experimental and computational study on multicomponent evaporation of diesel fuel droplets, Fuel 275 (2020) 117727.
[181] F. Lemoine, G. Castanet, Temperature and chemical composition of droplets by optical measurement techniques: a state-of-the-art review, Exp. Fluids 54 (7) (2013) 1572.
[182] Y. Zhao, H.H. Qiu, Measurements of multicomponent microdroplet evaporation by using rainbow refractometer and PDA, Exp. Fluids 40 (1) (2006) 60.
[183] S. Werner, W. Meier, Measurement of evaporation of hydrocarbon droplets by laser absorption spectroscopy, Appl. Phys. B 126 (1) (2020) 13.
[184] C.H. Jeong, H.J. Lee, D.Y. Kim, S.B. Ahangar, C.K. Choi, S.H. Lee, Quantitative analysis of contact line behaviors of evaporating binary mixture droplets using surface plasmon resonance imaging, Int. J. Heat Mass Transfer 165 (2021) 120690.
[185] C.H. Jeong, H.J. Lee, C.K. Choi, S.H. Lee, Selective evaporation rate modeling of volatile binary mixture droplets, Int. J. Heat Mass Transfer 178 (2021) 121584.
[186] S.K. Singh, S. Khandekar, D. Pratap, S.A. Ramakrishna, Wetting dynamics and evaporation of sessile droplets on nano-porous alumina surfaces, Colloids Surf. A 432 (2013) 71–81.
[187] M. Efstratiou, J. Christy, K. Sefiane, Crystallization-driven flows within evaporating aqueous saline droplets, Langmuir 36 (18) (2020) 4995–5002.
[188] C. Diddens, J.G. Kuerten, C.W.M. Van der Geld, H.M.A. Wijshoff, Modeling the evaporation of sessile multi-component droplets, J. Colloid Interface Sci. 487 (2017) 426–436.
[189] C. Diddens, Detailed finite element method modeling of evaporating multi-component droplets, J. Comput. Phys. 340 (2017) 670–687.
[190] E.L. Cussler, Diffusion: Mass Transfer in Fluid Systems, Cambridge University Press, 2009.
[191] A. Williams, Evaporation of Binary Liquids: Planar Layers and Sessile Drops (Doctoral dissertation), 2019, Retrieved from https://era.ed.ac.uk/handle/1842/35889.
[192] Z. Wang, G. Karapetsas, P. Valluri, A. Williams, K. Sefiane, Y. Takata, Dynamics of hygroscopic ionic solution droplets undergoing evaporation and vapor absorption, J. Fluid Mech. 912 (2021) A2, http://dx.doi.org/10.1017/jfm.2020.1073.
[193] J.P. Burelbach, S.G. Bankoff, S.H. Davis, Nonlinear stability of evaporating/condensing liquid films, J. Fluid Mech. 195 (1988) 463–494.
[194] M. Gad-El-Hak (Ed.), MEMS: Introduction and Fundamentals, CRC Press, 2005.
[195] B. González, N. Calvar, E. Gómez, Domínguez. Á, Surface tension of alcohol water+ water from 20 to 50. Degree. C, J. Chem. Eng. Data 40 (3) (1995) 611–614.
[196] S. Par, G. Guevara-Carrion, H. Hasse, J. Vrabec, Mutual diffusion in the ternary mixture of water+ methanol+ ethanol and its binary subsystems, Phys. Chem. Chem. Phys. 15 (11) (2013) 3985–4001.
[197] B. González, N. Calvar, E. Gómez, Á. Domínguez, Density, dynamic viscosity, and derived properties of binary mixtures of methanol or ethanol with water, ethyl acetate, and methyl acetate at T=(293.15, 298.15, and 303.15) K, J. Chem. Thermodyn. 39 (12) (2007) 1578–1588.
[198] A. Zuend, C. Marcolli, B.P. Luo, T. Peter, A thermodynamic model of mixed organic–inorganic aerosols to predict activity coefficients, Atmos. Chem. Phys. 8 (16) (2008) 4559–4593.
[199] A. Zuend, C. Marcolli, A.M. Booth, D.M. Lienhard, V. Soonsin, U.K. Krieger, D.O. Topping, G. McFiggans, T. Peter, J.H. Seinfeld, New and extended parameterization of the thermodynamic model AIOMFAC: calculation of activity coefficients for organic–inorganic mixtures containing carboxyl, hy-droxyl, carbonyl, ether, ester, alkenyl, alkyl, and aromatic functional groups, Atmos. Chem. Phys. 11 (17) (2011) 9155–9206.
[200] G. D'Errico, O. Ortona, F. Capuano, V. Vitagliano, Diffusion coefficients for the binary system glycerol+ water at 25 C. A velocity correlation study, J. Chem. Eng. Data 49 (6) (2004) 1665–1670.
[201] K. Takamura, H. Fischer, N.R. Morrow, Physical properties of aqueous glycerol solutions, J. Pet. Sci. Eng. 98 (2012) 50–60.
[202] N.S. Cheng, Formula for the viscosity of a glycerol- water mixture, Ind. Eng. Chem. Res. 47 (9) (2008) 3285–3288.
[203] P.S.Z. Rogers, K.S. Pitzer, Volumetric properties of aqueous sodium chloride solutions, J. Phys. Chem. Ref. Data 11 (1) (1982) 15–81.
[204] R.M. DiGuilio, Properties of lithium bromide-water solutions at high temperatures and concentrations-I. Thermal conductivity, ASHRAE Trans. 96 (1990) 702–708.
[205] J. Patek, J. Klomfar, A computationally effective formulation of the thermodynamic properties of LiBr–H_2O solutions from 273 to 500 K over full composition range, Int. J. Refrig. 29 (4) (2006) 566–578.
[206] V.S. Ajaev, Spreading of thin volatile liquid droplets on uniformly heated surfaces, J. Fluid Mech. 528 (2005) 279–296.
[207] G. Karapetsas, K.C. Sahu, O.K. Matar, Evaporation of sessile droplets laden with particles and insoluble surfactants, Langmuir 32 (27) (2016) 6871–6881.
[208] D.R. Beacham, O.K. Matar, R.V. Craster, Surfactant-enhanced rapid spreading of drops on solid surfaces, Langmuir 25 (24) (2009) 14174–14181.
[209] B.J. Fischer, Particle convection in an evaporating colloidal droplet, Langmuir 18 (1) (2002) 60–67.

[210] K.L. Maki, S. Kumar, Fast evaporation of spreading droplets of colloidal suspensions, Langmuir 27 (18) (2011) 11347–11363.
[211] R.V. Craster, O.K. Matar, K. Sefiane, Pinning, retraction, and terracing of evaporating droplets containing nanoparticles, Langmuir 25 (6) (2009) 3601–3609.
[212] E.B. Dussan, S.H. Davis, On the motion of a fluid-fluid interface along a solid surface, J. Fluid Mech. 65 (1) (1974) 71–95.
[213] P. Ehrhard, S.H. Davis, Non-isothermal spreading of liquid drops on horizontal plates, J. Fluid Mech. 229 (1991) 365–388.
[214] P.J. Haley, M.J. Miksis, The effect of the contact line on droplet spreading, J. Fluid Mech. 223 (1991) 57–81.
[215] L.M. Hocking, Rival contact-angle models and the spreading of drops, J. Fluid Mech. 239 (1992) 671–681.
[216] Y.D. Shikhmurzaev, Moving contact lines in liquid/liquid/solid systems, J. Fluid Mech. 334 (1997) 211–249.
[217] D.N. Sibley, N. Savva, S. Kalliadasis, Slip or not slip? A methodical examination of the interface formation model using two-dimensional droplet spreading on a horizontal planar substrate as a prototype system, Phys. Fluids 24 (8) (2012) 082105.
[218] J.H. Snoeijer, B. Andreotti, Moving contact lines: scales, regimes, and dynamical transitions, Annu. Rev. Fluid Mech. 45 (2013) 269–292.
[219] V.S. Ajaev, Spreading of thin volatile liquid droplets on uniformly heated surfaces, J. Fluid Mech. 528 (2005) 279–296.
[220] H.P. Kavehpour, B. Ovryn, G.H. Mckinley, Microscopic and macroscopic structure of the precursor layer in spreading viscous drops, Phys. Rev. Lett. 91 (19) (2003) 196104.
[221] A. Hoang, H.P. Kavehpour, Dynamics of nanoscale precursor film near a moving contact line of spreading drops, Phys. Rev. Lett. 106 (25) (2011) 254501.
[222] H. Xu, D. Shirvanyants, K. Beers, K. Matyjaszewski, M. Rubinstein, S.S. Sheiko, Molecular motion in a spreading precursor film, Phys. Rev. Lett. 93 (20) (2004) 206103.
[223] J.M. Gomba, G.M. Homsy, Analytical solutions for partially wetting two-dimensional droplets, Langmuir 25 (10) (2009) 5684–5691.
[224] J.M. Gomba, G.M. Homsy, Regimes of thermocapillary migration of droplets under partial wetting conditions, J. Fluid Mech. 647 (2010) 125–142.
[225] V.M. Starov, M.G. Velarde, Surface forces and wetting phenomena, J. Phys.: Condens. Matter 21 (46) (2009) 464121.
[226] P.G. De Gennes, Wetting: statics and dynamics, Rev. Modern Phys. 57 (3) (1985) 827.
[227] D. Bonn, J. Eggers, J. Indekeu, J. Meunier, E. Rolley, Wetting and spreading, Rev. Modern Phys. 81 (2) (2009) 739.
[228] V.M. Starov, M.G. Velarde Velarde, Wetting and Spreading Dynamics, CRC Press, 2019.
[229] A.H. Persad, C.A. Ward, Expressions for the evaporation and condensation coefficients in the Hertz-Knudsen relation, Chem. Rev. 116 (14) (2016) 7727–7767.
[230] J.M. Stauber, S.K. Wilson, B.R. Duffy, K. Sefiane, On the lifetimes of evaporating droplets with related initial and receding contact angles, Phys. Fluids 27 (12) (2015) 122101.
[231] P. Gurrala, P. Katre, S. Balusamy, S. Banerjee, K.C. Sahu, Evaporation of ethanol-water sessile droplet of different compositions at an elevated substrate temperature, Int. J. Heat Mass Transfer 145 (2019) 118770.
[232] T. Ozturk, H.Y. Erbil, Evaporation of water-ethanol binary sessile drop on fluoropolymer surfaces: Influence of relative humidity, Colloids Surf. A 553 (2018) 327–336.
[233] H.Y. Erbil, G. McHale, M.I. Newton, Drop evaporation on solid surfaces: constant contact angle mode, Langmuir 18 (7) (2002) 2636–2641.
[234] Z. Lu, M.H.K. Schaarsberg, X. Zhu, L.Y. Yeo, D. Lohse, X. Zhang, Universal nanodroplet branches from confining the ouzo effect, Proc. Natl. Acad. Sci. 114 (39) (2017) 10332–10337.
[235] L.A. Bawazer, C.S. McNally, C.J. Empson, W.J. Marchant, T.P. Comyn, X. Niu, et al., Combinatorial microfluidic droplet engineering for biomimetic material synthesis, Sci. Adv. 2 (10) (2016) e1600567.
[236] B. Ghosh, R. Bose, T. Tang, Can coacervation unify disparate hypotheses in the origin of cellular life? Curr. Opin. Colloid Interface Sci. 52 (2020) 101415.
[237] A. Molliex, J. Temirov, J. Lee, M. Coughlin, A.P. Kanagaraj, H.J. Kim, et al., Phase separation by low complexity domains promotes stress granule assembly and drives pathological fibrillization, Cell 163 (1) (2015) 123–133.
[238] A.G. Larson, D. Elnatan, M.M. Keenen, M.J. Trnka, J.B. Johnston, A.L. Burlingame, et al., Liquid droplet formation by HP1α suggests a role for phase separation in heterochromatin, Nature 547 (7662) (2017) 236–240.
[239] O.K. Matar, R.V. Craster, Models for marangoni drying, Phys. Fluids 13 (7) (2001) 1869–1883.